ELSEVIER

Contents lists available at ScienceDirect

Earth and Planetary Science Letters

journal homepage: www.elsevier.com/locate/epsl





A Great Tsunami Earthquake Component of the 1957 Aleutian Islands Earthquake

Yoshiki Yamazaki ^a, Thorne Lay ^b, Kwok Fai Cheung ^{a,*}, Robert C. Witter ^c, SeanPaul M. La Selle ^d, Bruce E. Jaffe ^d

- ^a Department of Ocean and Resources Engineering, University of Hawai'i at Mānoa, Honolulu, HI 96822, USA
- b Department of Earth and Planetary Sciences, University of California Santa Cruz, Santa Cruz, CA, 95064, USA
- ^c U.S. Geological Survey, Alaska Science Center, Anchorage, AK, 99508, USA
- ^d U.S. Geological Survey, Pacific Coastal and Marine Science Center, Santa Cruz, CA, 95060, USA

ARTICLEINFO

Keywords: Aleutian earthquakes megathrust coupling non-hydrostatic modeling tsunami deposits tsunami earthquakes tsunami hazards

ABSTRACT

The great 1957 Aleutian Islands earthquake ruptured \sim 1200 km of the plate boundary along the Aleutian subduction zone and produced a destructive tsunami across Hawai'i. Early seismic and tsunami analyses indicated that large megathrust fault slip was concentrated in the western Aleutian Islands, but tsunami waves generated by slip in the west cannot explain the large observed runup in Hawai'i far to the southeast. Recently mapped 1957 geologic deposits on eastern Aleutian Islands suggest occurrence of very large nearby slip. Jointly modeling tsunami runup along the eastern Aleutian and Hawaiian Islands together with tide gauge recordings across the Pacific resolves 12-26 m shallow slip along 600 km of the eastern Aleutian Islands in addition to modest, deeper western slip inferred from seismic records. The eastern near-trench slip results in an M_W 8.3-8.6 sunami earthquake component of the M_W 8.6-8.8 rupture, comparable in size to the adjacent 1946 Aleutian tsunami earthquake to the east. The reexamination of the 1957 rupture confirms the tsunami hazards posed by the eastern Aleutian subduction zone to Hawai'i and lays the groundwork for investigation of large prehistoric earthquakes through modeling tsunami runup inferred from stratigraphic observations to constrain their rupture processes.

1. Introduction

The Central North Pacific location of Hawai'i results in direct exposure to tsunamis generated at the Aleutian subduction zone along \sim 3000 km of the boundary between the Pacific and North America plates. Much of the subduction zone ruptured in several great earthquakes during the last century (Fig. 1). These include the 1946 M_W 8.6 Aleutian Islands, 1965 M_W 8.7 Rat Islands, and 1957 M_W 8.6±0.2 Aleutian Islands ruptures (Sykes, 1971; Sykes et al., 1980), all of which generated destructive tsunamis. The curvature of the Aleutian arc, combined with the strong trench-perpendicular radiation pattern for tsunamis produced by under-thrusting earthquakes, make the eastern Aleutian Islands along the 1946 and the eastern half of the 1957 rupture zones a primary potential tsunami source for Hawai'i (Butler, 2012; Butler et al., 2014, 2017). Models based on geodetic data suggest current creeping of the deeper plate boundary along Unimak Island and Unalaska Island and moderate slip deficit accumulation along Umnak Island (Fig. 1), but

geodetic observations have limited resolution of shallow megathrust coupling due to block motion of the upper plate and the large distance from the stations to the shallow plate boundary near the trench (Cross and Freymueller, 2008; Freymueller et al., 2008; Elliott and Freymueller, 2020). The phase in the earthquake cycle of the subduction zone further complicates interpretation of geodetic data for plate coupling given the time needed for detectable strain to accumulate after prior ruptures (Govers et al., 2017). This emphasizes the importance of historical record and prehistoric evidence of large earthquakes in the region for tsunami hazard assessment.

The 1946 rupture was a "tsunami earthquake", which generated an unusually large tsunami for its earthquake magnitude (Kanamori, 1972; Polet and Kanamori, 2000; Lay and Bilek, 2007). The faulting involved relatively slow slip of at least 8 m, and possibly much more, along the shallow plate boundary (Pelayo, 1990; López and Okal, 2006), in a region for which recent geodetic slip deficit is not detected (Li and Freymueller, 2018). The resulting tsunami produced 42 m runup at Scotch

E-mail address: cheung@hawaii.edu (K.F. Cheung).

^{*} Corresponding author.

Cap on Unimak Island as well as 10.4 m runup at Hā'ena, Kaua'i; 16.4 m in Waikolu Valley, Moloka'i; and 8.1 m in Hilo, Island of Hawai'i (López and Okal, 2006; Walker, 2004). This important event demonstrates the potential for strongly tsunamigenic shallow rupture in the eastern Aleutian Islands and severe tsunami impacts in Hawai'i as a consequence. The 9 March 1957 event, the second largest earthquake to strike the United States in the last 300 years and one of the eight largest earthquakes around the world since 1900, involved a much longer rupture than the adjacent 1946 event (Fig. 1), with an aftershock zone extending ~1200 km along the Aleutian arc (Sykes et al., 1980; Tape and Lomax, 2022). The tsunami produced runup of 16.2 m at Wainiha Bay, Kaua'i; 9.1 m at Ka'ena Point, O'ahu; and 4.3 m at Hilo, Island of Hawai'i (Walker, 2004). The non-uniform large-slip distributions inferred from modeling of early far-field seismic observations and near and far-field tide-gauge records were almost all placed in the western half of the aftershock zone (Johnson and Satake, 1993; Johnson et al., 1994), which faces westward from Hawai'i. The strong trench-perpendicular radiation of tsunami waves from a western Aleutian Arc rupture cannot account for the large runup observed along the Hawaiian Islands.

Field observations and tide gauge records from the eastern Aleutian Islands provide strong evidence for large tsunami excitation in the eastern portion of the 1957 rupture. Observed sandy tsunami deposits and drift logs extend 800 m inland to 18.5 m elevation at Stardust Bay, Sedanka Island and suggest runup exceeding 23 m at Driftwood Bay, Umnak Island (Witter et al., 2016; 2019). Wrack lines delineating highest debris deposits from the 1957 tsunami reach 32 m on Unalaska Island and 18 m on the Pacific side of Chuginadak Island, the largest of the Islands of Four Mountains (Griswold et al., 2019). Tsunami modeling from rupture offshore Unalaska Island requires approximately 20 m of

shallow slip to account for the Stardust Bay deposits as well as the tide gauge recording on the north side of Unalaska Island (Nicolsky et al., 2016). The tsunami also left behind sandy deposits and extensive runup evidence along the Hawaiian Islands that add to the already diverse observations (Walker 2004; La Selle et al., 2020). Griswold et al. (2019) combined 10 to 20 m uniform slip along the eastern Aleutian Islands at less than 15 km depth with western slip inferred from tide gauge records by Johnson et al. (1994) to explain features of the Aleutian Islands deposits as well as runup observations at two sites on Kaua'i. The inferred eastern rupture together with the western slip from earlier models suggests an M_W of 8.8-9.0 for the 1957 earthquake, approaching an estimate of 9.1 based on the total aftershock area (Kanamori, 1997); however, a self-consistent fault-slip distribution that can account for both seismic and tsunami records has not yet been published for the

We propose an improved rupture model for the 1957 earthquake that adopts prior seismological constraints from Johnson et al. (1994) on the faulting in the western rupture zone. Joint modeling of tsunami deposit and runup observations in the eastern Aleutian and Hawaiian Islands as well as tide gauge recordings across the Pacific provides constraints of slip in the eastern rupture zone. The tsunami modeling of Nicolsky et al. (2016) and Griswold et al. (2019) as well as the inferred long dislocation time resulting in weakened seismic wave excitation and a paucity of shallow aftershock activity adjacent to the 1946 rupture zone strongly suggest a tsunami earthquake component in the eastern Aleutian Islands. Modeling of near and far-field tsunami observations proves effective in differentiating slip from the shallow and deeper megathrust as well as constraining the extent and distribution along strike (Yamazaki et al., 2018; Bai et al., 2022). Reproduction of the diverse tsunami

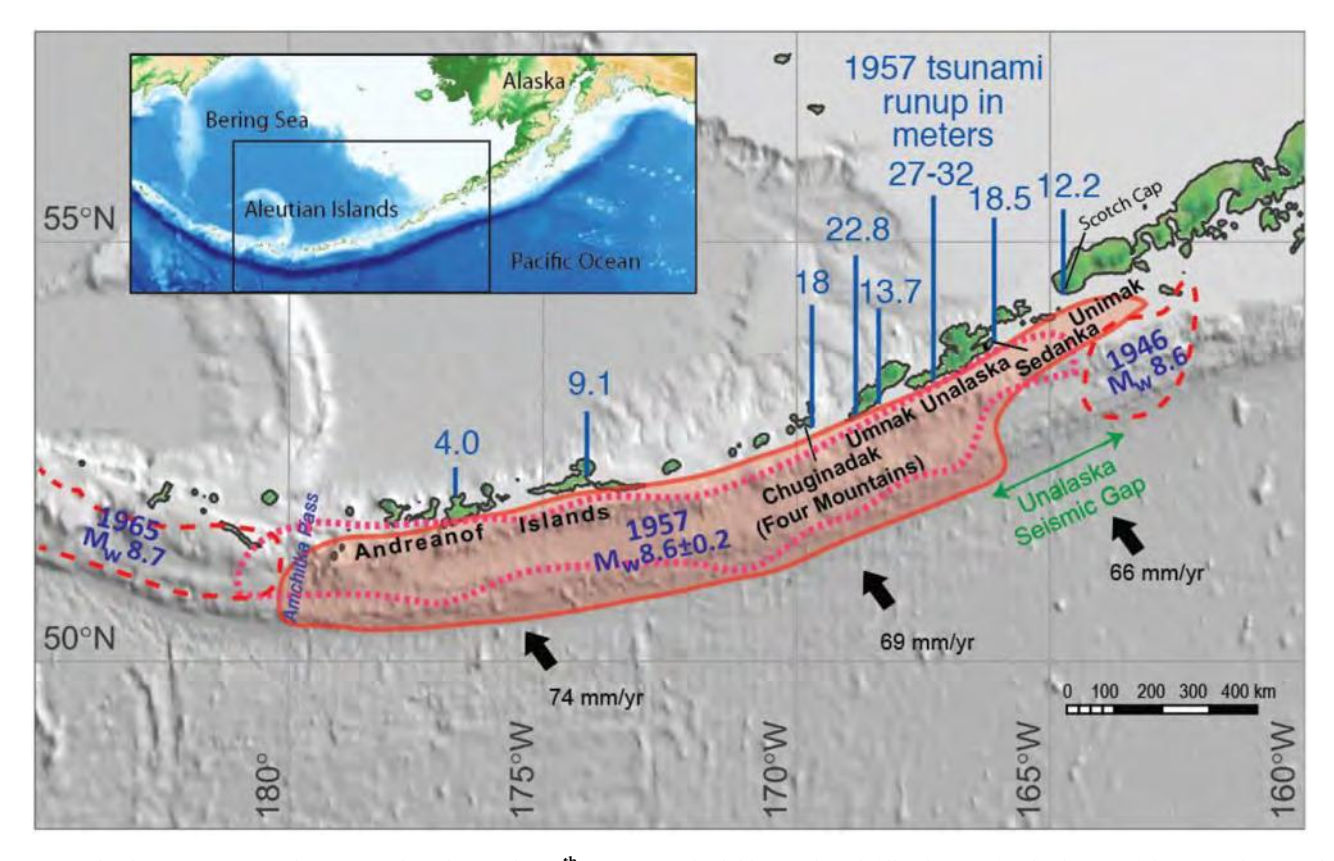


Fig. 1. Aftershock zones of great Aleutian earthquakes in the 20th century. Red solid line with pink fill indicates aftershock zone of the 1957 Aleutian Islands earthquake from Sykes et al. (1980), with the red dotted line indicating the relocated aftershock zone from Tape and Lomax (2022). Blue bars denote observed maximum runup from the resulting tsunami compiled by Nicolsky et al. (2016). Red dashed lines delineate relocated aftershock zones of the 1946 Aleutian Islands tsunami earthquake and the 1965 Rat Islands earthquake (Tape and Lomax, 2022). Arrows and labels indicate Pacific plate convergence direction and rate relative to a fixed North American/Bering Sea plate. The inset locates the map region along the Aleutian-Alaska plate boundary. The approximate extent of the proposed Unalaska seismic gap in the shallow megathrust of the eastern portion of the 1957 rupture zone is indicated in green (Sykes et al., 1980; House et al., 1981).

observations, especially when short-period waves from near-trench slip are involved, poses a challenge to commonly used shallow-water models for non-dispersive long waves. We utilize a non-hydrostatic approach to more precisely account for wave shoaling on continental and insular slopes and propagation across the ocean in fitting the tsunami observations, thereby minimizing model errors from being projected into the fault-slip distribution (Li et al., 2016; Yamazaki et al., 2023).

2. Tsunami Observations and Modeling

2.1. Tsunami Observations

The 1957 Aleutian Islands earthquake produced a destructive tsunami with tide gauge, geologic, and runup observations across the north Pacific that have not been fully utilized in prior studies of the event. Fig. 2 shows the locations of selected observations to constrain the fault-slip distribution through tsunami modeling. Along the Aleutian Islands, the observations include the Unalaska and Attu tide gauge records to the east and west of the epicenter as well as geologic records at Chuginadak Island, Driftwood Bay, and Stardust Bay along the easternmost 400 km of the aftershock zone (Witter et al., 2016, 2019; Griswold et al., 2019). The tsunami runup is estimated by the positions of drift logs stranded far inland and high above the shoreline. The logs are likely transported inland by tsunamis because no trees grow on the islands. Sandy deposits, recording the tsunami inundation, were examined in trenches and sediment cores, and described in the field. The positions of trenches, cores, and drift logs were measured using real-time kinematic Global Navigation Satellite System (RTK GNSS) survey instruments with ± 1.5 cm horizontal and ± 3 cm vertical accuracy. Elevations are referenced to the mean tide level, which is determined at each site from water level measurements using pressure transducers and the National Tidal Datum Epoch.

In the Hawaiian Islands, three north-facing coastal wetlands, Anahola, Kahana, and Pololū were surveyed for deposits of tsunamis (La Selle et al., 2020). Sandy deposits were examined in sediment cores, and described in the field. Handheld GPS units provided all core locations within a horizontal error of \pm 4 m. An RTK GNSS survey instrument was used to measure core elevations in Anahola Valley. Core elevations in Kahana and Pololū Valleys were inferred from LiDAR data. All site elevations refer to the local mean sea level. Independent runup observations are available near the three survey sites for validation of the modeled results (Walker, 2004). Additional runup comparisons are included for north Kaua'i in the direct path of tsunami waves originating from rupture immediately west of Chuginadak Island and near Hilo at the eastern end of the island chain because of its tide gauge record. The observed runup heights reference the local tide level during the 1957 tsunami, but in the absence of precise geographic measurements, their locations were interpreted from field notes and coalesced with any nearby historical observations for cataloging tsunami hazards around each island (Walker, 2004). The Aleutian and Hawai'i observations are supplemented by tide gauge records at Yakutat, Neah Bay, San Francisco, and Newport Bay along the North America west coast to provide 180° azimuth coverage of the tsunami.

2.2. Tsunami Modeling

The non-hydrostatic model NEOWAVE includes a depth-averaged vertical velocity term in the nonlinear shallow-water equations to describe tsunami generation from seafloor deformation, wavenumber-dependent shoaling on seafloor slopes, and frequency dispersion during trans-oceanic propagation (Yamazaki et al., 2009, 2011). The vertical inertia in the nonhydrostatic flow is important for accurate prediction of coastal runup on steep topography (Bai et al., 2023b). A shock-capturing scheme approximates breaking waves as bores or hydraulic jumps that can account for energy dissipation without predefined mechanisms or empirical coefficients. These model capabilities,





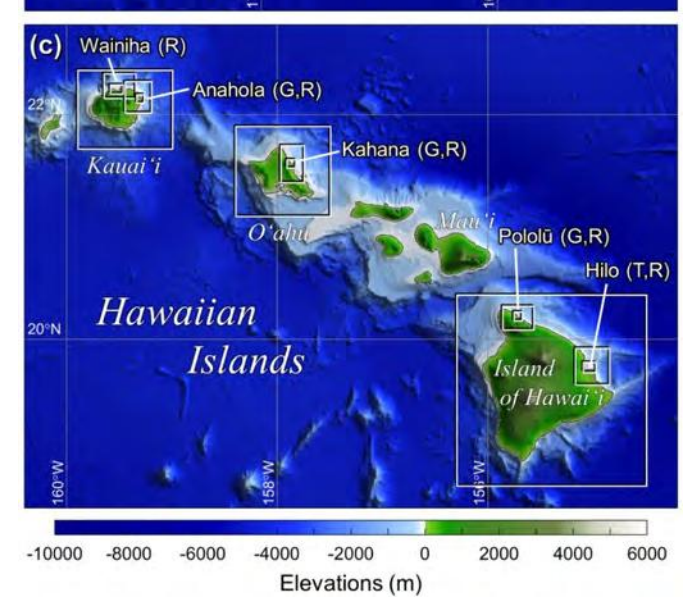


Fig. 2. Location map for tsunami observations and computational grids. (a) Level-1 and 2 grids for North Pacific and regional computations with epicenter (red star) and tide-gauge (T) locations. (b) Level-2 to 5 grids for eastern Aleutian Islands with additional geologic (G) record locations. (c) Level-2 to 5 grids for major Hawaiian Islands with additional runup (R) record locations.

which are important for reproduction of near and far-field wave dynamics, have been benchmarked against mathematical and numerical models as well as laboratory and field measurements (Yamazaki et al., 2023). The non-hydrostatic approach also provides a direct interface with fault-slip models for computation of tsunami generation. Implementation of prescribed subfault dislocation and rise time with an elastic half-space solution from Okada (1985) provides the time history of earth surface deformation. The vertical displacement is adjusted for horizontal translation of the local slope to update the digital elevation model and define the tsunami excitation (Tanioka and Satake, 1996), which is embedded in the seafloor kinematic boundary condition as forcing for the quasi three-dimensional flow.

The modeling involves up to five levels of two-way nested computational grids with increasing resolution to the selected sites with tide gauge, runup, and deposit observations of the tsunami generated by the 1957 Aleutian Islands earthquake (Fig. 2). The level-1 grid covers the north Pacific from Kamchatka to North America including Hawai'i. The 2-arcmin resolution gives rise to optimal dispersion properties in NEO-WAVE for modeling transoceanic propagation of tsunamis (Li and Cheung, 2019). A series of level-2 grids resolve the shelf and slope complex along the Aleutian Islands, the major Hawaiian Islands, and segments of the North America west coast at 30 arcsec. The level-3 to 5 grids telescope from 6 to 0.3 arcsec resolution at the observation sites, except for Chuginadak Island, which is resolved at 15 arcsec of the available bathymetry. Manning's numbers of 0.025 and 0.035 describe subgrid roughness of the seafloor and terrain consistent with recommendations from Kotani et al. (1998) and Bricker et al. (2015). The digital elevation model includes GEBCO for the Pacific Basin and high-resolution datasets for the Aleutian and Hawaiian Islands and US west coast available from NOAA NCEI. The local mean-sea level defines the datum of the digital elevation model as well as the initial sea-surface elevation for tsunami modeling.

2.3. Comparison of Model Results and Observations

The well-positioned tsunami deposits and runup observations in the eastern Aleutian and Hawaiian Islands are complementary for constraining 1957 coseismic rupture processes and allow reconciliation of modeled slip placement along strike and down dip. Tsunami deposits provide lower-bound estimates of runup. Prior studies have suggested a 1-m flow depth as the threshold to produce preservable sediment deposits (Namegaya and Satake, 2014). This serves as general guidance in matching modeled flow depth with the deposit records at the Aleutian sites, which are of central importance in constraining slip offshore. The Hawai'i runup observations compiled by Walker (2004) might be offset from the record locations and include maximum water heights on land, and that requires special attention when being fitted with modeled runup in supplementing the Aleutian deposits to infer the slip distribution. The tide range is 1.2 m at the Aleutian deposit sites and 0.6 m in Hawai'i and its effects are secondary in the much larger runup computed from the local mean sea level.

The tide-gauge records provide time information to complement the deposit and runup observations of the tsunami event. The leading wave amplitude can confirm the overall seismic displacement, while the phase allows assessment of the total rupture sequence and adds secondary constraints on the rupture length and depth. The arrival time, however, could be influenced by ocean-layer stratification and compressibility as described by Tsai et al. (2013) or instrumentation errors from ground shaking in the near field as observed by Cox (1980). Stilling-well tide gauges, which were commonly used at the time, are known to dampen and lag short-period tsunami signals resulting in smoother recorded waveforms (Satake et al., 1988). In addition, tide gauges might be relocated due to retrofitting or expansion of dock facilities. Their current locations and the harbor configurations used in the modeling might differ from those in 1957. The tide gauge records require careful interpretation when comparing with modeled results for validation of

rupture models inferred from the observed Aleutian and Hawai'i runup.

3. Model Results

3.1. Starting models from previous studies

We seek a fault-slip distribution for the 1957 Aleutian Islands earthquake through an iterative refinement procedure, which begins with published models from seismic and tide gauge data inversion (Johnson et al., 1994). Comparison of computed tsunamis with deposit, runup, and tide-gauge observations guides refinements to the fault-slip distribution for another round of computations until satisfactory agreement is achieved. Early models for the slip distribution were mapped onto our finite-fault grid (Figs. 3a and 3b), which includes 3 rows by 12 columns of subfaults representative of the megathrust interface geometry from Hayes (2018) along the 1957 aftershock zone (Fig. 1). The three rows of 100-km long subfaults with 30, 60, and 60 km width and 15° , 20° , and 25° dip correspond to the near-trench, central, and down-dip plate boundary depth ranges, classified as Domains A, B, and C (Fig. 3c), which tend to host tsunami, large-slip, and moderate-slip earthquakes across the megathrust, respectively (Fig. S1; Lay et al., 2012). For the eastern Aleutian arc, the upper plate crust in contact with the slab is confined to depths less than about 15 km, roughly corresponding to the 30-km along-dip Domain A. Seismic imaging has shown that low P velocities exist in the upper plate outer forearc along Domain A, whereas much higher velocities exist along the mantle/slab contact for deeper Domains B and C (e.g., Lizarralde et al., 2002). The finite-fault grid captures dominant features of the great earthquake in matching the available observations. A finer grid is used in joint modeling of higher-quality seismic and tsunami records to resolve time histories of fault-slip processes in greater detail for recent events (e.g., Bai et al., 2022, 2023a).

The seismic data are surprisingly limited for this event, but P-wave recordings indicate source radiation over at least 180 to 240 s prior to PP arrivals (Johnson et al., 1994), with no indication of very strong late arrivals. The three to four minutes of available signal likely do not span the entire source process for a fault rupturing 800 km eastward from the hypocenter. For a conventional rupture velocity of 2.5 km/s, the P-wave windows may only capture radiation from slip within 600 km or so from the hypocenter, so it is unclear whether there is later P-wave radiation. Inversions by Johnson et al. (1991) of tide gauge observations and of one of the few on-scale long-period seismic recordings of multiple great circle surface waves provided slip distributions approximated by tsunami-inferred model 1957-J1994-T in Fig. 3a and seismically inferred model 1957-J1994-S in Fig. 3b. We adopt full-width interface failure over 150 km for the tsunami-inferred model as in Johnson et al. (1994) and assume deeper, 120-km wide rupture for the seismically inferred model as is commonly observed for large interplate earthquakes. However, direct constraints on the along-dip rupture distribution are totally lacking from the seismic recording. Assuming an average rigidity of 37.5 GPa, model 1957-J1994-T has a seismic moment of 1.13×10^{22} Nm (M_W 8.64) and model 1957-J1994-S has half of that moment at 5.56 \times $10^{21}\,$ Nm (M_W 8.43). These early slip models locate almost all seismic moment and slip in the western half of the aftershock zone (Fig. 1).

NEOWAVE can model tsunami generation from rupture propagation as well as multiple faulting at different times (Bai et al. 2023a), but the observations do not provide good constraints on source rupture velocity. We assume 40 s rise time and simultaneous rupture to model the tsunami at sites with tide gauge, runup, and deposit observations. Fig. 4 shows the computed wave amplitude across the North Pacific and the tide-gauge signals comparison. The tide-gauge records from Johnson et al. (1994) and Nicolsky et al. (2016), which have arbitrary reference times or a notable offset from the earthquake time, are shifted to align with computed arrivals, as done in the prior studies. For both models in Fig. 3, the tsunami is strongest westward from Hawai'i with rapid reduction toward the east, where most of the observations are located.

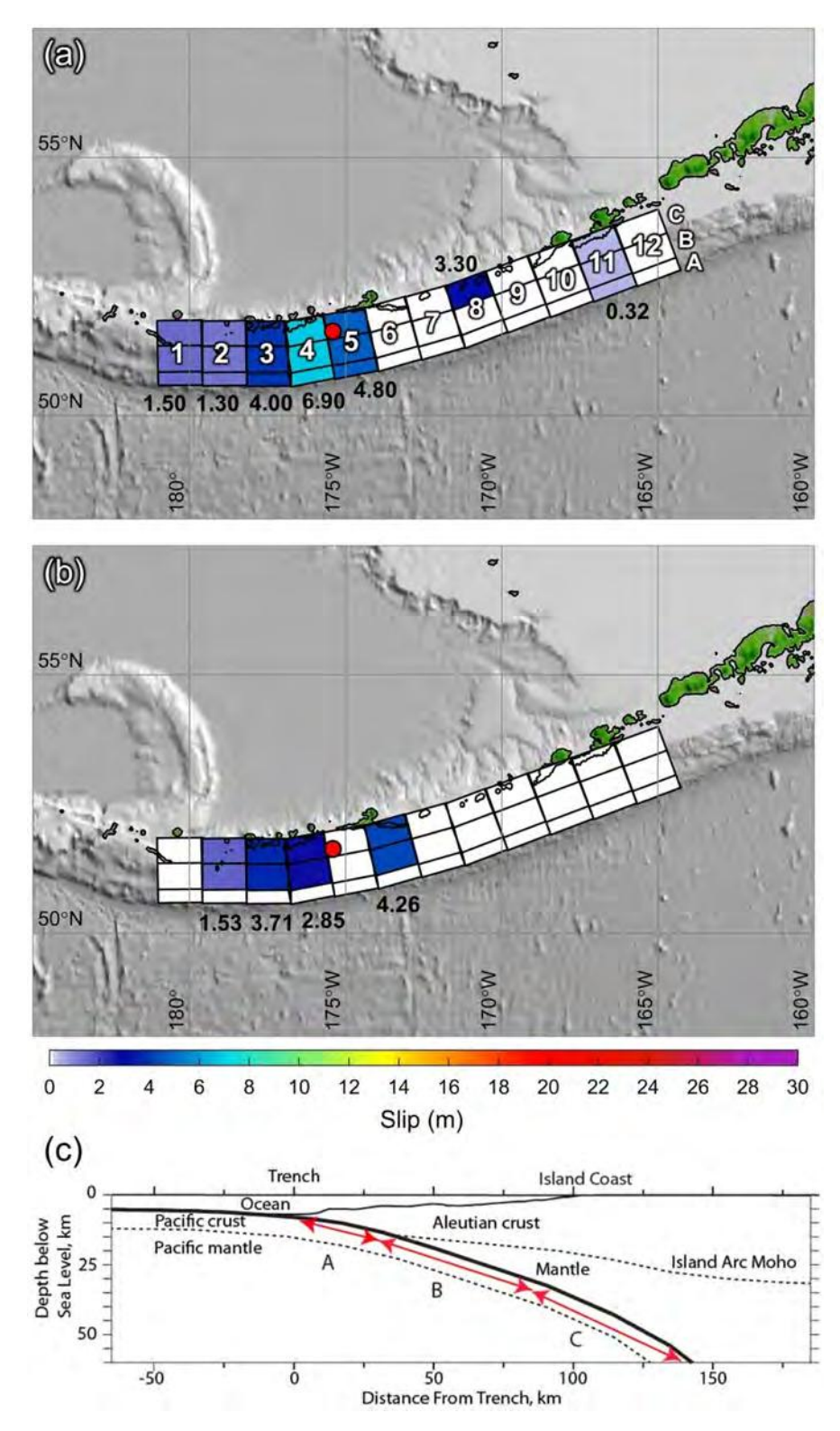


Fig. 3. Finite-fault grid and starting models for the 1957 Aleutian Islands earthquake. (a) Model 1957-J1994-T adapted from inversion of tide-gauge tsunami observations. (b) Model 1957-J1994-S adapted from inversion of a seismic record. Both models are based on Johnson et al. (1994) with uniform slip indicated by black labels and color-coded in meters. (c) Schematic cross-section scaled appropriately for the subduction zone. The red circle indicates the epicenter; labels 1-12 and A-C indicate columns and rows of subfaults 100 km along-strike and 30, 60 and 60 km wide down-dip.

The larger moment of the tsunami-inferred model generates more energetic waves (Fig. 4a), notably at the Attu and Unalaska tide gauges immediately west and east of the rupture, respectively (Fig. 4c). The predicted waveforms tend to overestimate the recorded amplitude and period at stations along the North America west coast. The Hilo

tide-gauge comparison shows the best agreement, whereas prior models with similar slip from Johnson and Satake (1993) and Johnson et al. (1994) under-predicted the amplitude by a factor of 2, likely due to low-resolution computations. The seismically inferred model gives improved agreement with the predominately long-period signals at Attu,

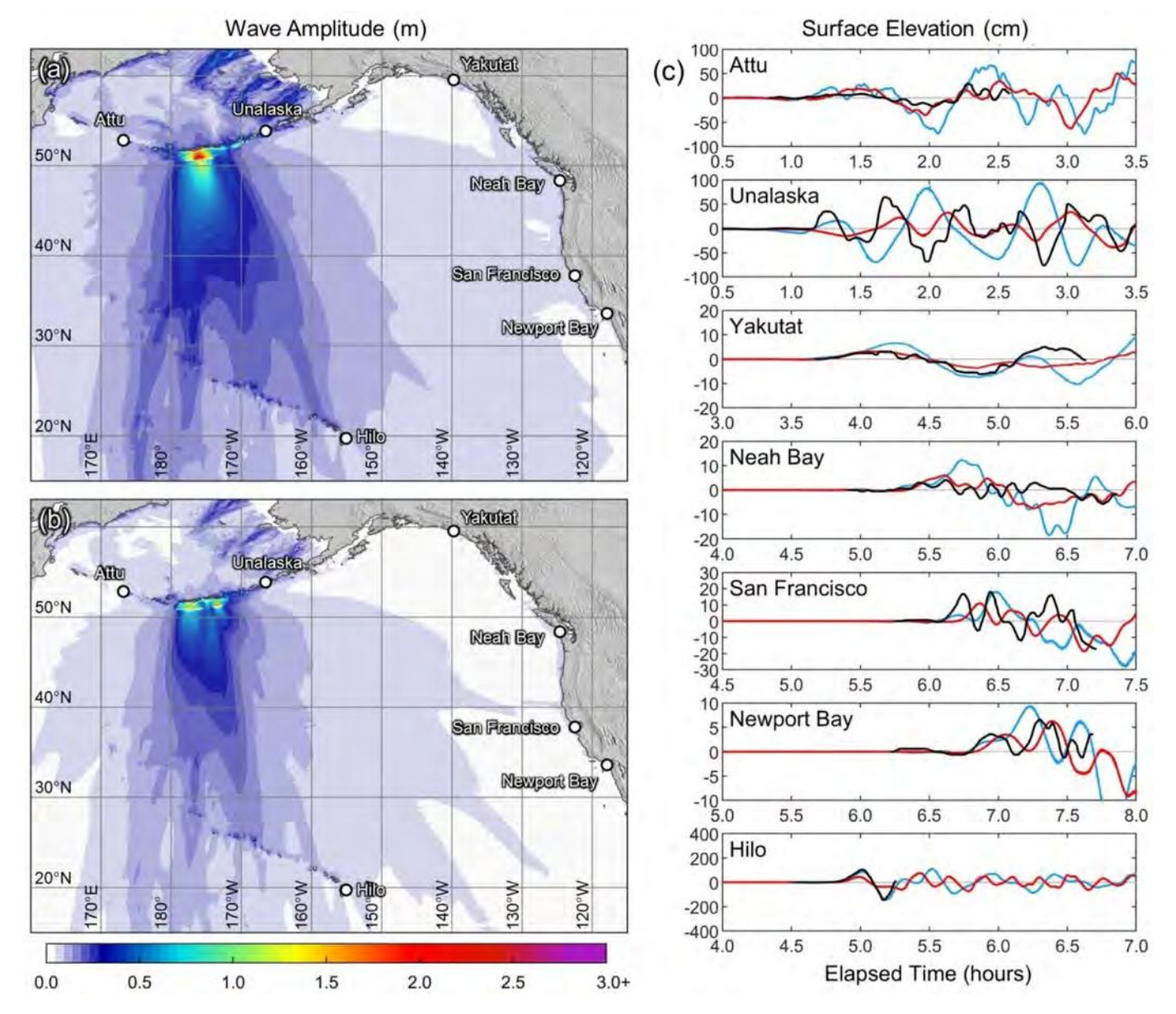


Fig. 4. Wave amplitude and tide-gauge waveforms from starting models. (a) Model 1957-J1994-T. (b) Model 1957-J1994-S. White circles indicate tide gauge locations. (c) Comparison of de-tided tsunami records (black) with computed waveforms from 1957-J1994-T (blue) and 1957-J1994-S (red). The tsunami records are shifted to align with the computed wave arrivals for direct comparison.

supporting the assumed deeper western rupture, but underestimates the records at Unalaska Island and Hilo. The less energetic waves for this model lead to more comparable results at the west coast tide gauges. Both models, which do not produce any inundation beyond the beach area, completely fail to reproduce runup and deposit observations in the eastern Aleutian and Hawaiian Islands (Figs. S2 and S3).

The poor comparison with observations east of the earthquake from both models confirms the need for tsunami excitation in the eastern aftershock zone. The observed large eastern Aleutian runup and weak late seismic radiation suggest a tsunami earthquake component with large near-trench slip that generates dispersive tsunami waves across the ocean. The tide-gauge waveform inversion underlying 1957-J1994-T is very likely distorted by the full-width subfaults and linear non-dispersive modeling used by Johnson et al. (1994). Li et al. (2016) showed a non-hydrostatic model with finer subfaults is necessary to resolve large near-trench slip of a tsunami earthquake. The seismically inferred 1957-J1994-S is not dependent on alignments or interpretations of tsunami data and its slip distribution within the western aftershock

zone is capable of reproducing the tsunami record at Attu to the west. Domain A ruptures in the eastern aftershock zone provide a viable explanation for the lack of late strong seismic waves as the low seismic velocities on the crust/slab contact can lower rupture velocity and slip velocity, yielding low P-wave radiation even for very large slip. Preliminary modeling indicated that Domain A ruptures can reconcile runup observations along the Aleutian and Hawaiian Islands more readily than deeper Domain B or C ruptures, or wider Domain A+B or A+B+C ruptures. We therefore start our iterative modeling using 1957-J1994-S as a base model and seek simple fault-slip distributions in the shallow eastern aftershock zone that match the deposit, runup, and tide gauge observations with the lowest seismic moment.

3.2. Preferred model from iterative refinement

The tsunami computation was iterated through 51 fault-slip models in matching the observations under the assumption of simultaneous rupture. Each model includes the western rupture from seismic wave inversion (Johnson et al., 1994), but varies the Domain A slip in the six eastern near-trench subfaults. Fig. 5 shows four selected fault-slip models to illustrate the range of uncertainties in along-strike slip placement. The large near-trench slip in the eastern rupture zone enhances the computed runup to match the observed deposits in the Aleutian Islands and results in dispersion across the ocean to reproduce the far-field observations. The easternmost 200 km segment at subfaults 11A and 12A is well constrained by tsunami deposits on the gradually steepening valley slope at Stardust Bay. The range of permissible slip increases at subfault 10A due to presence of a ledge at the landward limit of tsunami deposits at Driftwood Bay, where the computed inundation becomes less sensitive to the slip. The low-resolution digital elevation model at Chuginadak Island also reduces the sensitivity of the computed runup to offshore slip at subfault 9A. Models 1957-Y2023-A and 1957-Y2023-B in Figs. 5a and 5b span the upper and lower bounds of slip uncertainties along 400 km of near-trench rupture constrained by the Aleutian deposits alone. There is no local constraint on any shallow slip west of Chuginadak Island, but the large observed runup on north Kaua'i complements the near-field observations. Models 1957-Y2023-C and D in Figs. 5c and 5d respectively include 100 and 200-km westward extensions of the near-trench rupture to demonstrate sensitivity of the computed north Kaua'i runup as well as slip reconciliation within the longer rupture in maintaining the match with the near-field deposit observations.

The four models produce a wide range of runup on north Kaua'i, but

comparable results at other sites, demonstrating the solution space and range of uncertainties among Domain A ruptures. The wave-amplitude plots in Figs. 6a and 6b illustrate the tsunami radiation pattern for models 1957-Y2023-C and 1957-Y2023-D with 500 and 600 km long eastern ruptures, respectively. The latter, preferred model gives slightly better overall agreement with the tide gauge observations in Fig. 6c (See Movie S1 for tsunami propagation). The longer eastern rupture energizes a sidelobe toward Kaua'i, while having little effect on the main lobe and the diffracted waves to the east and west. The computed waveform at Attu is primarily generated by the western rupture inferred from seismic data with minor contributions from the eastern rupture $\sim\!2$ hours after initial arrival. At Unalaska Island, the signals from the western rupture are considerable (Fig. 4c), and their constructive and destructive interference with the shorter period waves arriving simultaneously from the eastern near-trench slip gives very good agreement with the recorded waveform. The precise phase alignment validates the slip placement in both western and eastern rupture zones and suggests their faulting occur within a relatively short time interval that can be approximated as simultaneous in the tsunami modeling. The Yakutat tide gauge located far to the east recorded diffracted waves with good match of the initial arrival from the eastern rupture. The computed, subsequent arrivals include diffracted waves from abrupt slip transitions across subfaults. The tide gauge at Neah Bay, Washington, recorded the long-period diffracted waves along with short-period oscillations of the semi-enclosed embayment, while the tide gauges farther south,

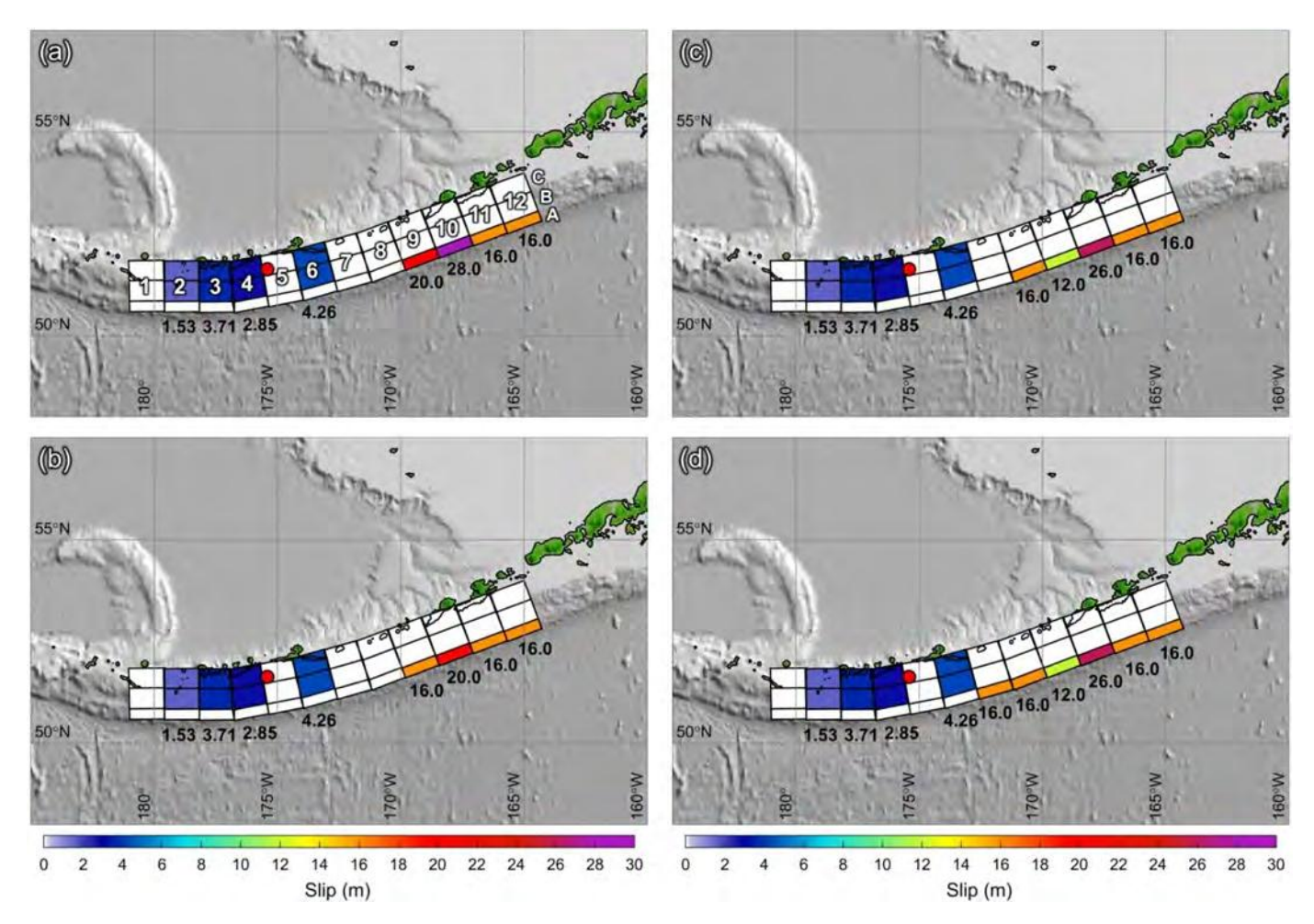


Fig. 5. Model 1957-J1994-S augmented with large eastern shallow slip. (a) Models 1957-Y2023-A. (b) Model 1957-Y2023-B. These two models represent upper and lower-bound shallow slip along 400 km of rupture constrained by Aleutian deposit records (Witter et al., 2019; Griswold et al., 2019). (c) Model 1957-Y2023-C. (d) Model 1957-Y2023-D. These two models have 500 and 600 km long shallow rupture and reconciled slip distributions to fit additional, north Kaua'i runup observations in Hawai'i (Walker 2004). The red circle indicates the epicenter; white numerals and alphabets indicate columns and rows of subfaults 100 km along-strike and 30, 60 and 60 km wide down-dip. Uniform slip regions with amount indicated by black labels are color-coded in meters.

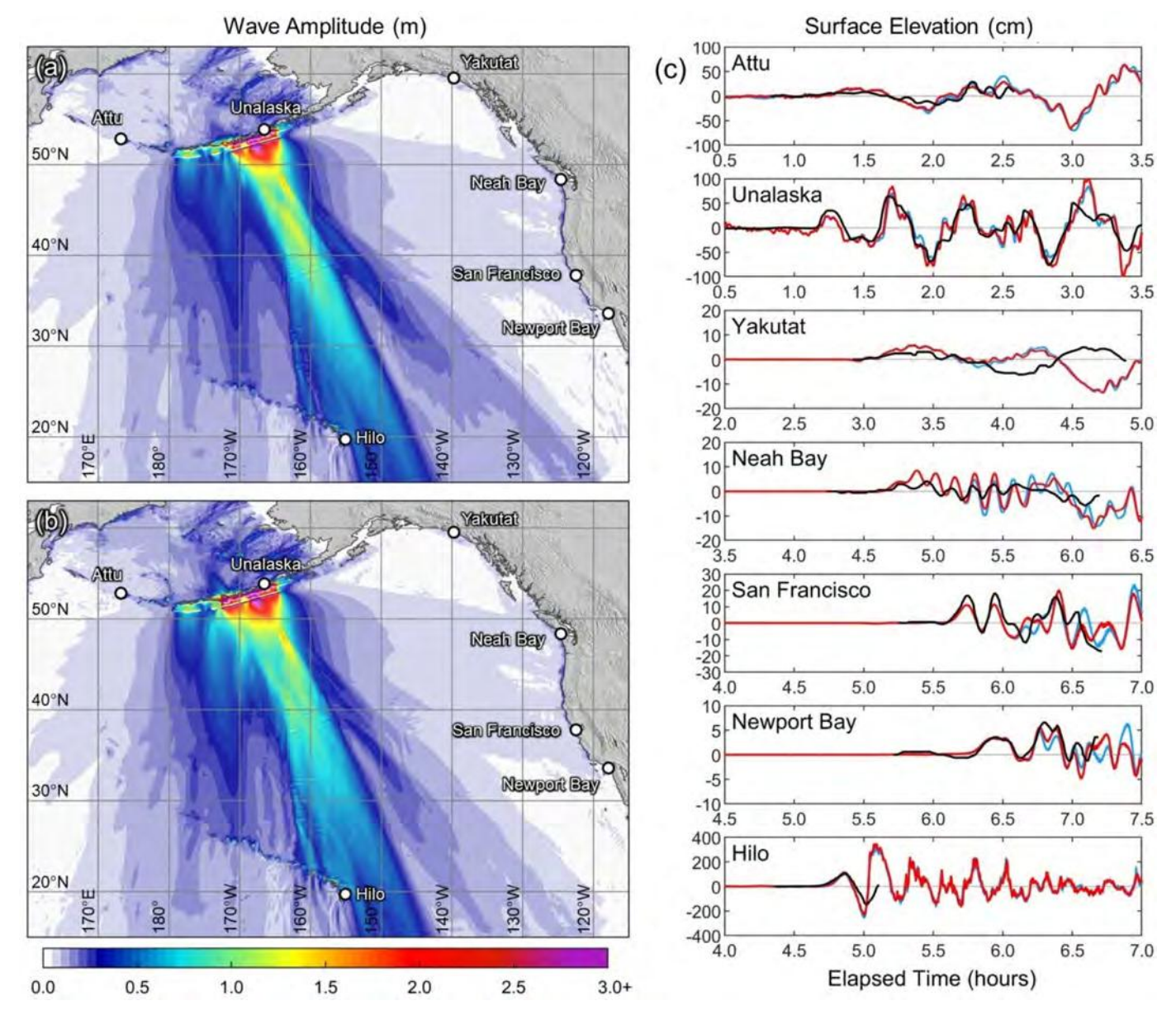


Fig. 6. Wave amplitude and tide-gauge waveforms from converging models. (a) Model 1957-Y2023-C. (b) Model 1957-Y2023-D. White circles indicate tide gauge locations. (c) Comparison of tsunami records (black) with waveforms from models 1957-Y2023-C (blue) and 1957-Y2023-D (red). The tsunami records are shifted to align with the computed wave arrivals for direct comparison.

including Hilo in Hawai'i, recorded shorter period signals from radiated waves influenced by dispersion. These recorded time series are well reproduced by modeled waves arriving sequentially from the eastern and western ruptures with 7 min lag time at Hilo, 30 min at Newport Bay and San Francisco, California, and 40 min at Neah Bay.

The tsunami impacts along the Aleutian and Hawaiian Islands are strongly influenced by shelf processes dependent on the dominant wave period or indirectly the slip placement along dip. The large shallow slip in the eastern rupture produces an elongated, narrow initial sea-surface pulse through a strongly non-hydrostatic process at the wedge toe and its descent and rebound over the deep trench generate short-period waves that shoal and refract more effectively over submarine ridges and canyons to produce localized impacts (Fig. 7a). The landward propagating tsunami waves are amplified by the rebound from initial sea-surface drawdown caused by seafloor subsidence (Movie S1). The computed signals at the Unalaska tide gauge in Fig. 6c shows that the non-hydrostatic model is able to resolve the tsunami waves from the trench without spurious short-period oscillations as seen in shallow-

water model results (Nicolsky et al., 2016). The shorelines with amplified wave action correspond well with locations showing large runup observations in Fig. 1. These include the location with 32 m runup and the three sites with observed tsunami deposits at high elevation (Witter et al., 2019; Griswold et al., 2019). The offshore propagating tsunami transforms into a wave packet with a leading crest followed by a deep trough and dispersive waves with decreasing amplitude and period (Movie S1). The wave packet resonates over the interconnected insular shelves along the Hawaiian Islands (Fig. 7b). The amplification pattern closely follows the shelf and inter-island oscillation modes deduced by Cheung et al. (2013) and shows good correlation with large runup observations from Walker (2004), in particular, at Wainiha on the north Kaua'i. Anahola, Kahana, Pololū, and Hilo experience moderate wave action in comparison, but have observed runup and independent deposit data from La Selle et al. (2020) or tide gauge records for cross-validation of model results.

The computed inundation and runup for the preferred model 1957-Y2023-D are compared with observations. The three Aleutian sites

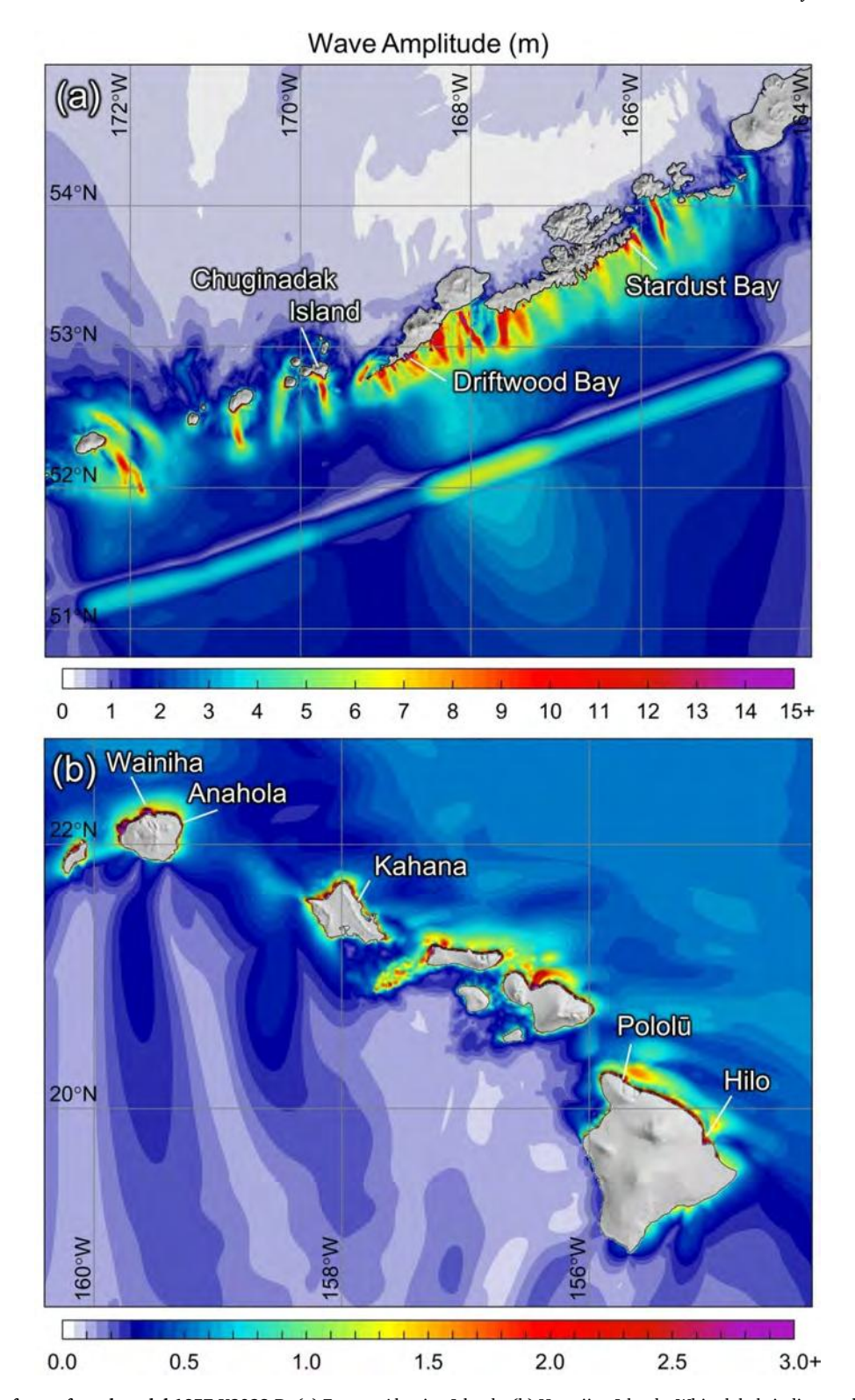


Fig. 7. Wave amplitude for preferred model 1957-Y2023-D. (a) Eastern Aleutian Islands. (b) Hawaiian Islands. White labels indicate selected sites with tsunami observations for high-resolution inundation and runup modeling.

provide primary constraints of slip at the four easternmost near-trench subfaults (Fig. 8a). The largest slip of 26 m in the partially locked region along Umnak Island is needed to match the Driftwood Bay deposits at elevations up to 23 m, and the slip reaches 16 and 12 m to the east and west, where only minor geodetic slip deficit is detected (Cross and Freymueller, 2008; Xue and Freymueller, 2020). The 16-m near-trench slip fronting Stardust Bay is consistent with the estimate from

localized tsunami modeling (Nicolsky et al., 2016), while the 12 m slip to the west is needed to account for the $7{\sim}18$ m runup on south Chuginadak Island (Griswold et al., 2019). The rupture extends 200 km west of Chuginadak Island to increase the radiation of tsunami energy toward Kaua'i. The short-period tsunami waves rapidly amplify over the near-shore reef and reproduce the large observed runup on steep slopes, but generate moderate flooding over the relatively flat alluvial and

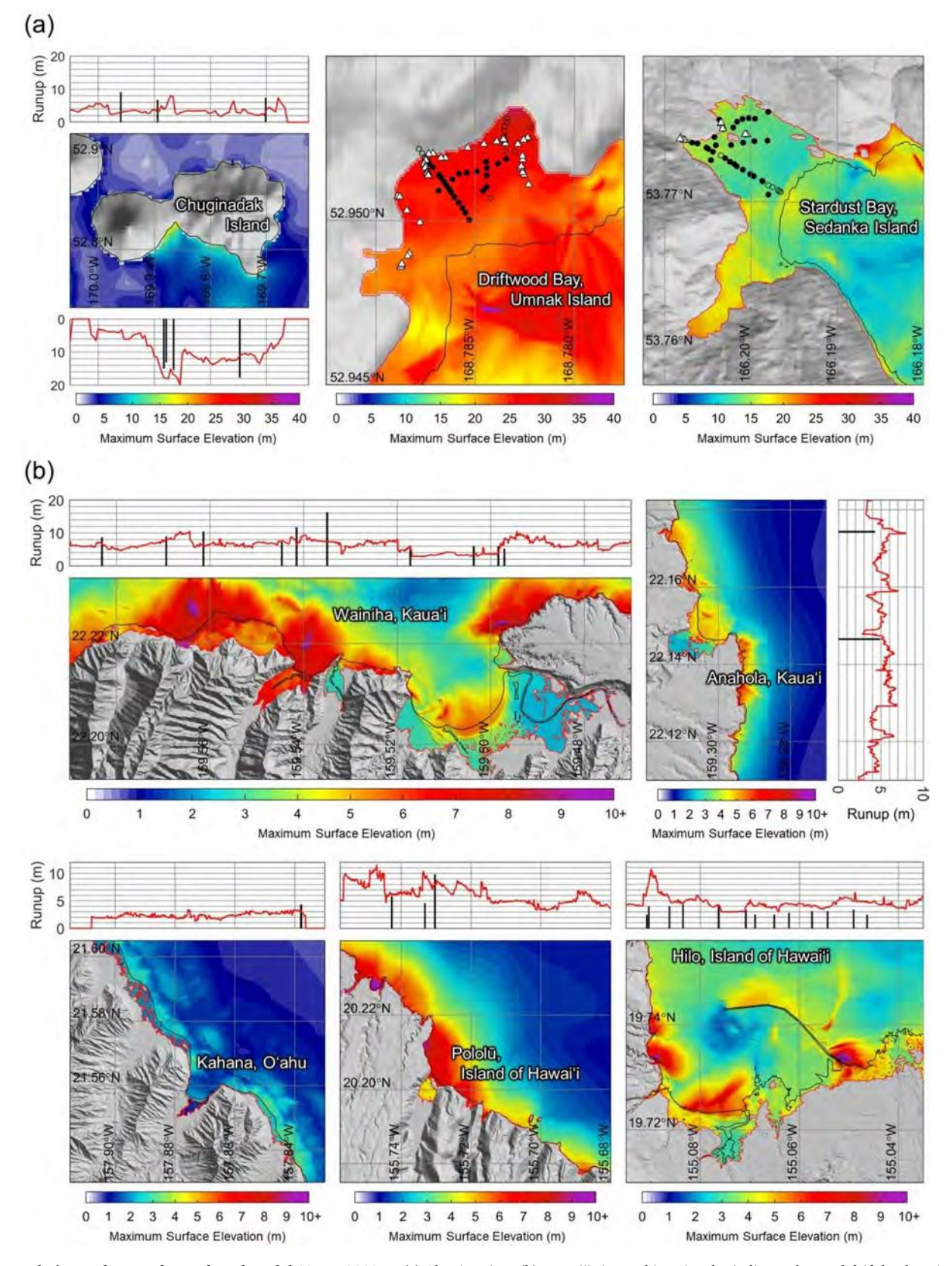


Fig. 8. Inundation and runup for preferred model 1957-Y2023-D. (a) Aleutian sites. (b) Hawai'i sites. White triangles indicate observed drift log locations; solid and open black circles denote cores with and without deposits. Black bars denote observed maximum deposit elevations on Chuginadak Island from Griswold et al. (2019) and observed runup heights at Hawai'i sites from Walker (2004). Black lines denote waterlines at local MSL and red lines delineate computed runup heights and inundation limits.

coastal plains at the five Hawai'i sites (Fig. 8b). Computed flow-depth discontinuities at the shore suggest collapse of tsunami bores onto the coastal plain as sheet flows with considerable energy dissipation. The observed runup on Kaua'i's north shore is instrumental in constraining the 16-m slip west of Chuginadak Island, which only has secondary effects at other sites (Fig. S4). The runup observations at Hilo suggest some overestimation of the modeled impact despite good agreement of the computed and recorded leading crest at the tide gauge (Fig. 6c). This is likely caused by excess local resonance on the insular slope (Bai et al., 2018), as indicated by the rapid and large drawdown after the initial arrival. The computed steep drawdown is triggered by a deep trough following the leading crest that is augmented by the negative phase of wave diffraction across abrupt slip transitions at the source (Movie S1). Minor discrepancies in the diverse data comparisons are expected for the simplified fault-slip model and the observation uncertainties.

3.3. Threshold for Tsunami Deposits

The observed runup heights on north Kaua'i and deposits on three eastern Aleutian Islands provide the primary constraints for the eastern slip distribution, which together with the western rupture inferred from seismic records, provides good overall agreement with tide gauge observations of the 1957 Aleutian tsunami. The self-consistency among the diverse observations adds confidence to the use of the 1-m flow depth threshold from Namegaya and Satake (2014) as general guidance in matching the computed tsunami inundation with the Driftwood and Stardust deposits (Fig. 9a). Both Aleutian sites, which together record nine tsunamis in the past two millennia (Witter et al., 2016; 2019), experience inundation from the open shore with abundant sediment supply and preservable deposits across the valley. The 1-m flow depth threshold, however, might not be applicable to Hawai'i with distinct physical environments, flow dynamics, and weather patterns. Tsunami

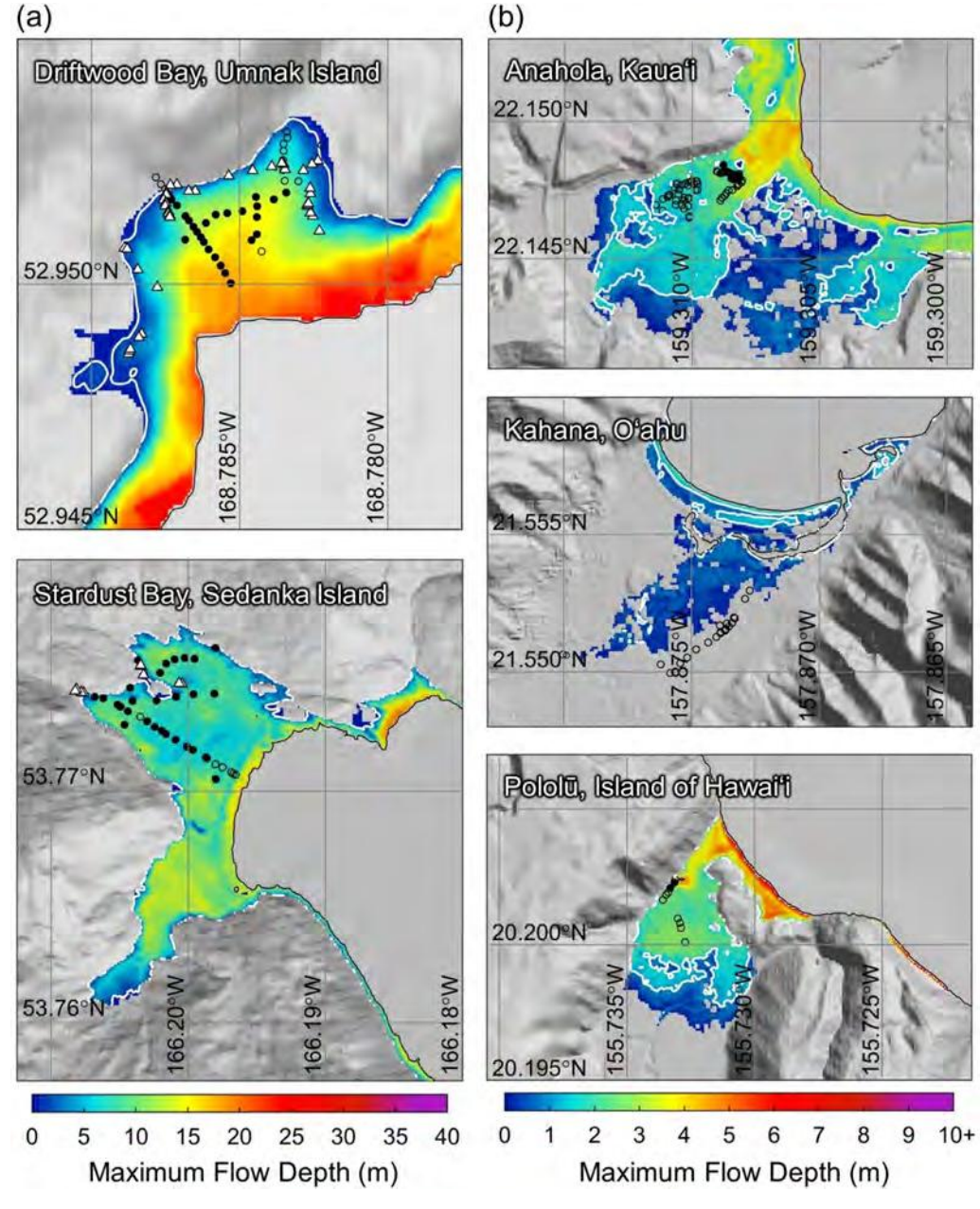


Fig. 9. Tsunami deposit record and flow depth for preferred model 1957-Y2023-D. (a) Aleutian sites. (b) Hawai'i sites. White triangles indicate observed drift log locations; solid and open black circles denote cores with and without deposits; black lines denote waterlines at local MSL and white lines are contours of 1-m flow depth.

deposits preserved from the 1957 event were observed at Anahola, Kaua'i, and Pololū, Island of Hawai'i, where deposits of a 14th century tsunami were also observed (La Selle et al., 2020). A sandy 1957 deposit was not observed in cores from Kahana Valley, O'ahu. All three sites also have independent runup observations from 1957 for local validation of the model results that in turn facilitates a closer examination of the computed flow depth with the deposit records (Fig 9b).

The model results at Kahana show floodwaters entering and spreading through a river channel onto the alluvial plain. All the cores, which have no detectable sandy deposits from the 1957 tsunami, are located outside the computed flood zone. The adjacent shoreline has less than 3 m of computed runup (Fig. 8b), which is postulated as a local threshold for tsunami deposit preservation (Chagué-Goff et al., 2012). Anahola and Pololū Valleys have similar general morphologies with a main channel on the north side adjacent to steep valley walls and coastal dunes to the southeast along the shore. The floodwaters entering though the main channels at the valleys inundate all the 1957 deposit locations; however, the core locations without deposits also experience up to 3~4 m flow depth. These values are subject to grid resolution and model uncertainties, but with the good agreement of nearby runup (Fig. 8b), unequivocally point to a flow-depth threshold greater than 1 m for these localities. Without overtopping and significant erosion of the sand dunes at Anahola and Pololū, the apparent higher threshold for preservable deposits could be due to supply of sediment limited to the channel mouth and adjacent shore as well as their location in alluvial plains subject to freshwater runoff or channel overflow during wet seasons. Hawai'i beaches typically comprise a layer of predominantly calcareous or basaltic sand mantling a shallow-reef substrate with distinct transport characteristics (Smith and Cheung, 2003, 2004). The tropical reef environment, in some cases, may limit the amount of sandy sediment transported inland by tsunamis (Apotsos et al., 2011).

4. Discussion and Conclusions

Tsunamis from the eastern Aleutian subduction zone remain a continuing threat to coastal communities in Hawai'i. A rational assessment of the tsunami hazard requires knowledge of the earthquake cycle and rupture pattern across the megathrust. The 1957 great Aleutian earthquake stretching $\sim \! 1200$ km along the Aleutian Arc is the most recent major event that can shed some light on these complex processes. The preponderance of evidence suggests the tsunami is primarily the result of shallow megathrust rupture, but tsunamigenic seafloor motion could also be produced by splay faults or submarine slumps, or some combination of multiple sources as has been proposed for the 1946 event (e.g., Lopez and Okal, 2006). While the available data do not rule out alternate sources for the tsunami, the present non-hydrostatic modeling unambiguously favors a 600 km long stretch of the eastern Aleutian Islands being a primary source of the very large tsunami. This is comparable to the 950 km long zone impacted by the 1907 Sumatra tsunami earthquake (Kanamori et al., 2010; Martin et al., 2019), but exceeds the rupture length of all well-documented recent tsunami earthquakes. It is very unlikely that synchronous upper plate faulting or slumping could have occurred over such a huge length. Lacking any evidence to clearly favor such alternatives and given the aftershock activity for a very long rupture along the megathrust, we discuss the proposed faulting scenario in terms of regional tectonics and historical events to further address its validity and implication.

The tsunami deposit and runup observations in the Aleutian and Hawaiian Islands are complementary in deducing the considerable coseismic slip in the near-trench region during the 1957 earthquake. The resulting dispersive tsunami waves are not amenable to early inversion of tide-gauge records with hydrostatic modeling and subfaults spanning the megathrust width (Johnson and Satake, 1993; Johnson et al., 1994). Previously published seismic models indicate a western rupture region with absence of the eastern shallow slip suggesting that the late source process indicated by the tsunami observations was relatively slow.

Assuming a long dislocation time and low rupture velocity in shallow, low seismic velocity material along Domain A (e.g., Lizarralde et al., 2002); it is straightforward to account for the lack of strong seismic excitation from the eastern portion of the rupture. The paucity of shallow aftershock activity adjacent to the 1946 rupture zone suggests a tsunami earthquake component of the great 1957 rupture. The available data do not resolve whether the near-trench region failed in the western Aleutian Islands. The assumed deeper, western rupture with clear seismic signals is corroborated by tide gauge recordings in the Aleutian Islands, but the up-dip limit of slip is not robustly constrained. The good fit to the overall time histories from tide-gauge stations favors a continuous event for the western and eastern ruptures. The duration of Pwave ground motions from the handful of on-scale recordings suggests source duration of at least 180 s (Johnson et al., 1994), but the data are insufficient to constrain the total duration and overall rupture velocity as well as the space-time history of slip.

The seismic moment for the eastern shallow slip in the preferred model 1957-Y2023-D is 1.15×10^{22} Nm (M_W 8.64), assuming a rigidity of 37.5 GPa, and the full model including the western rupture gives a moment of 1.70 \times 10²² Nm (M_W 8.75) for the 1957 event. The observed seismic waves show relatively uniform amplitudes for several hundred seconds (Johnson et al., 1994). Even with a rupture area 2.7 times larger in the west, early waves excited by the 1.5-4.3 m slip from deep on the fault are comparable to or larger than any later waves excited by the 12-26 m slip in the east from shallow faulting. Given the low seismic velocity along the crust/slab contact in the eastern Aleutian Islands (Lizarralde et al., 2002), it is plausible that the shallow megathrust rigidity is lower, as has been inferred for many events (Cheung et al., 2022). The seismic moment of the eastern portion could be as much as a factor of 2 to 4 lower as a result. Lowering the rigidity in the eastern, large shallow slip region by a factor of 3 reduces the seismic moment to 3.83×10^{21} Nm (M_W 8.32) and the total event moment to 9.39×10^{21} Nm (M_W 8.58). Very large shallow slip in the 2011 M_W 9.1 Tohoku earthquake appears to have accompanied larger down-dip slip (Lay, 2017), but this is probably not the case at least in the eastern portion of the 1957 rupture as any significant slip on the mantle/slab contact would produce strong seismic waves in the record due to increased velocities and rigidity.

The aftershock distribution of the 1957 event lacks activity in the near-trench region at the easternmost part of the rupture (Fig. 1), and this arguably played a role in proposing a shallow seismic gap off Unalaska Island west of the 1946 rupture zone (Sykes et al., 1980; House et al., 1981). It now appears that the large near-trench slip released shallow strain accumulated in the centuries prior to 1957, but did not produce shallow megathrust aftershock activity (Sykes et al., 1980; Tape and Lomax, 2022), similar to other tsunami earthquakes. The purported Unalaska seismic gap is not a seismic gap at all (Witter et al., 2016, 2019; Nicolsky et al., 2016). The observed, current strain deficit could be explained by strong locking in Domain A (Xue and Freymueller, 2020). Our simplified fault model cannot resolve any upper slip limits in Domains B and C with the available observations, but given the very large slip needed in Domain A, we cannot rule out deeper slip in the eastern portion of the 1957 rupture. While geodetic data do not resolve much current strain accumulation on the Domain B and C regions of the megathrust along Unalaska Island (Cross and Freymueller, 2008; Freymueller et al., 2008; Xue and Freymueller, 2020), it is unclear whether large slip events can occur there.

In the context of large slip zones from recent earthquakes in the Aleutian-Alaska megathrust (Fig. 10), the large eastern rupture of the 1957 earthquake was similar to the shallow, tsunami-earthquake in 1946, both of which account for the damaging waves observed in Hawai'i, while the western portion was akin to deeper slip in the 1986, 1996, 2020, and 2021 earthquakes (e.g., Boyd and Nabelek, 1988; Tanioka and González, 1998; Bai et al., 2022; Liu et al., 2023). There is no clear indication of shallow rapid slip up-dip of any of the latter zones, notably for the 1986 and 1996 events, which support our choice of

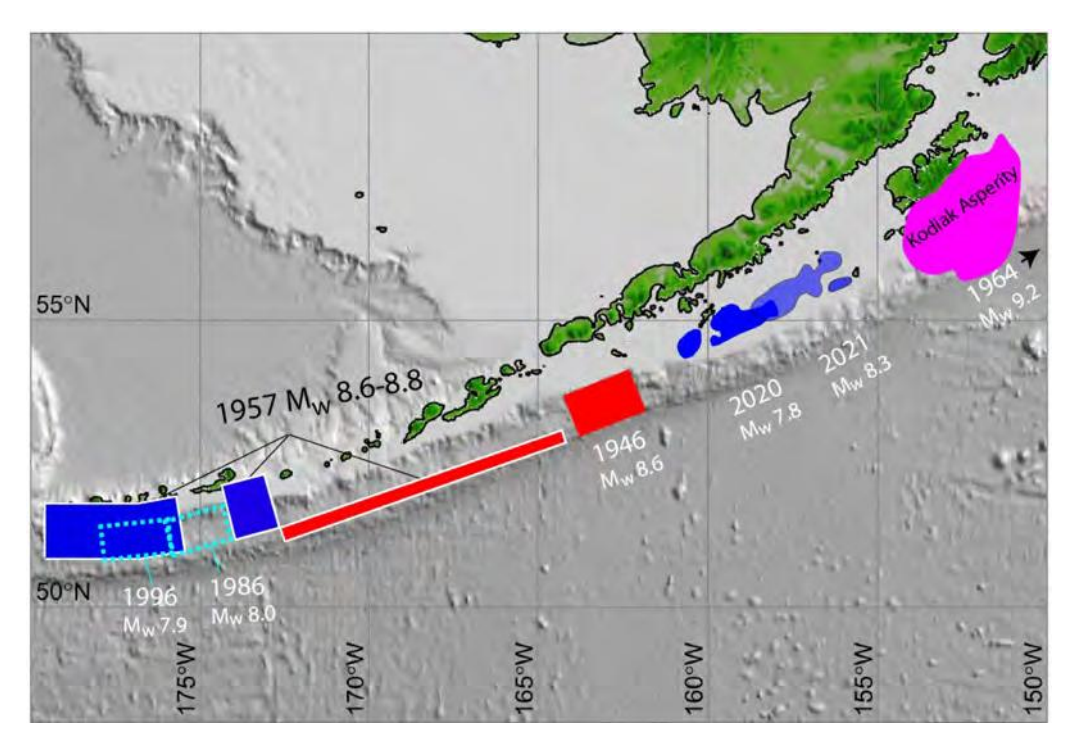


Fig. 10. Large-slip regions for major interplate earthquakes along the Aleutian Islands and Alaska Peninsula. The region of the Kodiak asperity with slip > 4 m is the western portion of the 1964 Alaska earthquake rupture model from Ichinose et al. (2007). The magenta coloring indicates rupture of Domains A, B, and C in that event. The 2020 Simeonof and 2021 Chignik source regions have > 0.5 and 2 m slip, respectively (Liu et al., 2023; Bai et al., 2022). Those two events ruptured Domains B and C and are colored blue. The 1946 large-slip zone from López and Okal (2006) is colored red because it may have ruptured Domains A and B. The 1986 source region with > ~2 m slip from Boyd and Nabelek (1998) and the 1996 earthquake large-slip zone from Tanioka and González (1998) are in Domain B. The large-slip patches in the western part of the 1957 rupture are colored blue because they possibly ruptured Domains B and C, whereas the eastern part of the 1957 rupture is colored red because it ruptured Domain A and appears to have been a tsunami earthquake component. The tsunami earthquake portions of the 1957 and 1946 earthquakes present the greatest hazard to Hawai'i (Butler et al., 2014, 2017).

limiting western slip in 1957 to Domains B and C. The 2021 earthquake overlapped the 1938 rupture zone, but there is uncertainty in whether shallow slip had occurred earlier (Johnson and Satake, 1994; Freymueller et al., 2021). The western asperity of the 1964 earthquake south of Kodiak Island does appear to have extended to the trench (Suito and Freymueller, 2009), with rupture across Domains A, B, and C. It remains to be established what causes the variable rupture depth extent along strike for recent events in the Aleutian-Alaska arc. Large amounts of sediment are entering the trench along Alaska and the Alaska Peninsula, but nonetheless the up-dip limit of rupture is observed to vary in the recent ruptures. Less sediment is entering the trench along the Aleutian Islands, but there are also variations in the up-dip limit of slip as inferred for the 1957 rupture. Fluids on the megathrust (e.g., Cordell et al., 2023), roughness of the plate interface (e.g., Liu et al., 2023), and other factors may play a role in delimiting along-dip seismic rupture.

The 1957 event can now be characterized as a compound earthquake involving rupture of the entire crust/slab interface at depths less than 15 km in the eastern Aleutian Islands and deeper slip along the mantle/slab interface in the western Aleutian Islands. Comparing this event with recent large tsunamigenic earthquakes reinforces the interpretation that occurrence of shallow slip during 1957 produced the 32-m maximum water height observed on Unalaska Island (Fig. S5). The improved understanding of the 1957 rupture provides strong testimonial to the value of field observations and records of tsunami waves from older earthquakes, confirming the major tsunami hazard for Hawai'i from the eastern Aleutian Islands. With the general methodology benchmarked for the 1957 earthquake and tsunami in this study, deduction of prehistoric events through modeling of the Aleutian and Hawai'i stratigraphic records from Witter et al. (2016; 2019) and La Selle et al. (2020) is the best prospect to extend the earthquake slip history and establish whether the deeper mantle/slab interface can host major ruptures along

the eastern Aleutian subduction zone.

CRediT authorship contribution statement

Yoshiki Yamazaki: Validation, Software, Methodology, Investigation, Formal analysis, Data curation, Conceptualization, Visualization, Writing – review & editing. Thorne Lay: Writing – review & editing, Writing – original draft, Validation, Software, Methodology, Investigation, Conceptualization, Formal analysis. Kwok Fai Cheung: Writing – review & editing, Writing – original draft, Supervision, Resources, Project administration, Methodology, Investigation, Funding acquisition, Conceptualization. Robert C. Witter: Investigation, Data curation, Writing – review & editing. SeanPaul M. La Selle: Investigation, Data curation, Writing – review & editing. Bruce E. Jaffe: Investigation, Writing – review & editing.

Declaration of competing interest

The authors declare that they have no known competing financial interests or personal relationships that could have appeared to influence the work reported in this paper.

Data availability

Data will be made available on request.

Acknowledgments

This study was supported by the National Tsunami Hazard Mitigation Program under National Oceanic and Atmospheric Administration

grant number NA20NWS467006 to the University of Hawai'i via Hawai'i Emergency Management Agency. T. Lay was supported by the National Science Foundation under grant number EAR-1802364. Funding for R. Witter, S. La Selle, and B. Jaffe came from the USGS Earthquake Hazards Program and the USGS Coastal and Marine Hazards and Resources Program. Guy Gelfenbaum, Jean-Philippe Avouac, Jeff Freymueller, and an anonymous referee provided insightful reviews of the manuscript. Any use of trade, firm, or product names is for descriptive purposes only and does not imply endorsement by the U.S. Government. SOEST Contribution No. 11765.

Supplementary materials

Supplementary material associated with this article can be found, in the online version, at doi:10.1016/j.epsl.2024.118691.

References

- Apotsos, A., Gelfenbaum, G., Jaffe, B., Watt, S., Peck, B., Buckley, M., Stevens, A., 2011. Tsunami inundation and sediment transport in a sediment-limited embayment on American Samoa. Earth-Sci. Rev. 107 (1-2), 1–11.
- Bai, Y., Liu, C., Lay, T., Cheung, K.F., Yamazaki, Y., 2023a. Fast and slow intraplate ruptures during the 19 October 2020 magnitude 7.6 Shumagin earthquake. Nature Comm 14 (1), 2015.
- Bai, Y., Liu, C., Lay, T., Cheung, K.F., Ye, L., 2022. Optimizing a model of coseismic rupture for the 22 July 2020 M_W 7.8 Simeonof earthquake by exploiting acute sensitivity of tsunami excitation across the shelf break. J. Geophys. Res.: Solid Earth 127 e2022/B024484.
- Bai, Y., Yamazaki, Y., Cheung, K.F., 2018. Amplification of drawdown and runup over Hawaii's insular shelves by tsunami N-waves from mega Aleutian earthquakes. Ocean Modell 124, 61–74.
- Bai, Y., Yamazaki, Y. Cheung, K.F., 2023b. Intercomparison of hydrostatic and nonydrostatic modeling for tsunami inundation mapping. Phys. Fluids 35 (7), 077111
- Boyd, T.M., Nabelek, J.L., 1988. Rupture process of the Andreanof Islands earthquake of May 7, 1986. Bull. Seismol. Soc. Am. 78, 1653–1673.
- Bricker, J.D., Gibson, S., Takagi, H., Imamura, F., 2015. On the need for larger Manning's roughness coefficients in depth-integrated tsunami inundation models. Coastal Eng. J. 57 (2), 1550005-1.
- Butler, R., 2012. Re-examination of the potential for great earthquakes along the Aleutian island arc with implications for tsunamis in Hawaii. Seis. Res. Lett. 83, 20, 39
- Butler, R., Burney, D.A., Walsh, D., 2014. Paleotsunami evidence on Kaua'i and numerical modeling of a great Aleutian tsunami. Geophys. Res. Lett. 41, 6795–6802.
- Butler, R., Walsh, D., Richards, K., 2017. Extreme tsunami inundation in Hawai'i from Aleutian-Alaska subduction zone earthquakes. Nat. Haz. 85, 1591–1619.
- Cheung, K.F., Bai, Y., Yamazaki, Y., 2013. Surges around the Hawaiian Islands from the 2011 Tohoku tsunami. J. Geophys. Res. Oceans 118 (10), 5703–5719.
- Cheung, K.F., Lay, T., Sun, L., Yamazaki, Y., 2022. Tsunami size variability with rupture depth. Nat. Geosci. 15, 33–36.
- Chagué-Goff, C., Goff, J., Nichol, S.L., Dudley, W., Zawadzki, A., Bennett, J.W., Mooney, S.D., Fierro, D., Heijnis, H., Dominey-Howes, D., Courtney, C., 2012. Multiproxy evidence for trans-Pacific tsunamis in the Hawaiian Islands. Mar. Geol. 299–302, 77–89.
- Cordell, D., Naif, S., Evans, R., Key, K., Constable, S., Shillington, D., Bécel, A., 2023. Forearc seismogenesis in a weakly coupled subduction zone influenced by slab mantle fluids. Nat. Geosci. 16, 822–827.
- Cox, D.C., 1980. Source of the tsunami associated with the Kalapana (Hawai'i) earthquake of November 1975. Institute for Marine and Atmospheric Research, University of Hawai'i, Honolulu.
- Cross, R.S., Freymueller, J.T., 2008. Evidence for and implications of a Bering plate based on geodetic measurements from the Aleutians and western Alaska. J. Geophys. Res. 113, B07405.
- Elliott, J., Freymueller, J., 2020. A block model of present-day kinematics of Alaska and western Canada. J. Geophys. Res.: Solid Earth 125 e2019JB018378.
- Freymueller, J.T. et al., 2008. Active deformation processes in Alaska, based on 15 years of GPS measurements, in Active Tectonics and Seismic Potential of Alaska. Geophysical Monograph Series, vol. 179, edited by J. T. Freymueller et al., AGU, Washington, D. C., pp. 1-42.
- Freymueller, J., Suleimani, E., Nicolsky, D.J., 2021. Constraints on the slip distribution of the 1938 M_W 8.3 Alaska peninsula earthquake from tsunami modeling. Geophys. Res. Lett. 48 e2021GL092812.
- Govers, R., Furlong, K.P., van de Wiel, L., Herman, M.W., Broerse, T., 2017. The geodetic signature of the earthquake cycle at subduction zones: Model constraints on the deep processes. Rev. Geophys. 56, 6–49. https://doi.org/10.1002/2017RG000586
- processes. Rev. Geophys. 56, 6–49. https://doi.org/10.1002/2017RG000586.
 Griswold, F.R., MacInnes, B.T., Higman, B., 2019. Tsunami-based evidence for large eastern Aleutian slip during the 1957 earthquake. Quat. Res. 91, 1045–1058.
- Hayes, G.P., 2018. Slab2, a comprehensive subduction zone geometry model. Science 362, 58–61.
- House, L.S., Sykes, L.R., Davies, J.N., Jacob, K.H., 1981. Identification of a possible seismic gap near Unalaska Island, eastern Aleutians, Alaska. In Earthquake

- Prediction An International Review. In: Simpson, D.W., Richards, P.G. (Eds.), Maurice Ewing Series, no. 4. AGU, Washington, D.C., pp. 81–92
- Ichinose, G., Somerville, P., Thio, H.-K., Graves, R., O'Connell, D., 2007. Rupture process of the 1964 Prince William Sound, Alaska, earthquake from the combined inversion of seismic, tsunami, and geodetic data. J. Geophys. Res. 112, B07306.
- Johnson, J.M., Satake, K., 1993. Source parameters of the 1957 Aleutian earthquake from tsunami waveforms. Geophys. Res. Lett. 20, 1487–1490.
- Johnson, J.M., Satake, K., 1994. Rupture extent of the 1938 Alaskan earthquake as inferred from tsunami waveforms. Geophys. Res. Lett. 21, 733–736.
- Johnson, J.M., Tanioka, Y., Ruff, L.J., Satake, K., Kanamori, H., Sykes, L.R., 1994. The 1957 great Aleutian earthquake. Pure Appl. Geophys. 142, 3–28.
- Kanamori, H., 1972. Mechanism of tsunami earthquakes. Phys. Earth Planet. Int. 6, 346–359.
- Kanamori, H., 1997. The energy release in great earthquakes. J. Geophys. Res. 82, 2981–2987
- Kanamori, H., Rivera, L., Lee, W.H.K., 2010. Historical seismograms for unraveling a mysterious earthquake: The 1907 Sumatra earthquake. Geophys. J. Int. 183, 358–374
- Kotani, M., Imamura, F., Shuto, N., 1998. Tsunami run-up simulation and damage estimation using GIS. Proc. Coast. Eng., JSCE 45, 356–360 in Japanese.
- La Selle, S., et al., 2020. Sedimentary evidence of prehistoric distant-source tsunamis in the Hawaiian Islands. Sediment 67, 1249–1273.
- Lay, T., 2017. A review of the rupture characteristics of the 2011 Tohoku-oki M_W 9.1 earthquake. Tectonophysics 733, 4–36.
- Lay, T., Bilek, S.L., 2007. Anomalous earthquake ruptures at shallow depths on subduction zone megathrusts. In: Dixon, T.H., Moore, J.C. (Eds.), The Seismogenic Zone of Subduction Zone Thrust Faults. Columbia University Press, New York, pp. 476–511.
- Lay, T., et al., 2012. Depth-varying rupture properties of subduction zone megathrust faults. J. Geophys. Res.: Solid Earth 117, B04311.
- Li, L., Cheung, K.F., 2019. Numerical dispersion in non-hydrostatic modeling of longwave propagation. Ocean Modell 138, 68–87.
- Li, L., Cheung, K.F., Yue, H., Lay, T., Bai, Y., 2016. Effects of dispersion in tsunami Green's functions and implications for joint inversion with seismic and geodetic data: A case study of the 2010 Mentawai M_W 7.8 earthquake. Geophy. Res. Lett. 43 (21), 11.182-11.191.
- Li, S., Freymueller, J.T., 2018. Spatial variation of slip behavior beneath the Alaska Peninsula along Alaska-Aleutian subduction zone. Geophys. Res. Lett. 45, 3453–3460.
- Liu, C., Bai, Y., Lay, T., Feng, Y., Xiong, X., 2023. Megathrust complexity and the up-dip extent of slip during the 2021 Chignik, Alaska Peninsula earthquake. Tectonophysics 854, 229808.
- Lizarralde, D., Holbrook, W.S., McGeary, S., Bangs, N., Diebold, J., 2002. Crustal construction of a volcanic arc, wide-angle seismic results from the western Alaska Peninsula. J. Geophys. Res. 107 (B8), 2164.
- López, A.M., Okal, E.A., 2006. A seismological reassessment of the source of the 1946 Aleutian 'tsunami' earthquake. Geophys. J. Int. 165, 835–849.
- Martin, S.S., Li, L., Okal, E.A., Morin, J., Tetteroo, A.E.G., Switzer, A.D., Sieh, K.E., 2019. Reassessment of the 1907 Sumatra "tsunami earthquake" based on macroseismic, seismological, and tsunami observations, and modeling. Pure. Appl. Geophys 176, 2831–2869.
- Namegaya, Y., Satake, K., 2014. Reexamination of the A.D. 869 Jogan earthquake size from tsunami deposit distribution, simulated flow depth and velocity. Geophys. Res. Lett. 41, 2297–2303.
- Nicolsky, D.J., et al., 2016. Evidence for shallow megathrust slip across the Unalaska seismic gap during the great 1957 Andreanof Islands earthquake, eastern Aleutian Islands. Alaska. Geophys. Res. Lett. 43, 10,328-10,337.
- Okada, Y., 1985. Surface deformation due to shear and tensile faults in a half-space. Bull. Seismol. Soc. Am. 75 (4), 1125–1154.
- Pelayo, A.M., 1990. Earthquake source parameter inversion using body and surface waves: applications to tsunami earthquakes and to Scotia Sea seismotectonics. Ph.D. Thesis. Washington University, St. Louis, p. 254.
- Polet, J., Kanamori, H., 2000. Shallow subduction zone earthquakes and their tsunamigenic potential. Geophys. J. Int. 142, 684–702.
- Satake, K., Okada, M., Abe, K., 1988. Tide gauge responses to tsunamis: Measurements at 40 tide gauge stations in Japan. J. Mar. Res. 46, 557–571.
- Smith, D.A., Cheung, K.F., 2003. Settling characteristics of calcareous sand. J. Hydraul. Eng. 129 (6), 469–483.
- Smith, D.A., Cheung, K.F., 2004. Initiation of motion of calcareous sand. J. Hydraul. Eng. 130 (5), 467–472.
- Suito, H., Freymueller, J.T., 2009. A viscoelastic and afterslip postseismic deformation model for the 1964 Alaska earthquake. J. Geophys. Res. 114, B11404.
- Sykes, L.R., 1971. Aftershock zones of great earthquakes, seismicity gaps, and earthquake prediction for Alaska and the Aleutians. J. Geophys. Res. 76, 8021–8041.
- Sykes, L.R., Kisslinger, J.B., House, L.S., Davies, J.N., Jacob, K.H., 1980. Rupture zones of great earthquakes in the Alaska-Aleutian arc, 1784 to 1980. Science 210, 1343–1345.
- Tanioka, Y., González, F.I., 1998. The Aleutian earthquake of June 10, 1996 (M_W 7.9) ruptured parts of both the Andreanof and Delarof segments. Geophys. Res. Lett. 25 (12), 2245–2248.
- Tanioka, Y., Satake, K., 1996. Tsunami generation by horizontal displacement of ocean bottom. Geophys. Res. Lett. 23 (8), 861–864.
- Tape, C., Lomax, A., 2022. Aftershock regions of Aleutian-Alaska megathrust earthquakes, 1938–2021. J. Geophys. Res.: Solid Earth 127. https://doi.org/ 10.1029/2022JB024336 e2022JB024336.

- Tsai, V.C., Ampuero, J.P., Kanamori, H., Stevenson, D.J., 2013. Estimating the effect of earth elasticity and variable water density on tsunami speeds. Geophys. Res. Lett. 40, 492-496. https://doi.org/10.1002/grl.50147.
 Walker, D., 2004. Regional Tsunami evacuations for the state of Hawaii: A feasibility
- study on historical runup data. Sci. Tsunami Hazards 22 (1), 3-22.
- Witter, R.C., et al., 2016. Unusually large tsunamis frequent a currently creeping part of the Aleutian megathrust. Geophys. Res. Lett. 43, 76-84.
- Witter, R.C., et al., 2019. Evidence for frequent, large tsunamis spanning locked and creeping parts of the Aleutian megathrust. Geolog. Soc. Am. Bull. 131, 707-729.
- Xue, X., Freymueller, J.T., 2020. A 25-year history of volcano magma supply in the east central Aleutian arc. Alaska. Geophys. Res. Lett. 47 e2020GL088388.
- Yamazaki, Y., Bai, Y., Goo, L.L., Cheung, K.F., Lay, T., 2023. Nonhydrostatic modeling of tsunamis from earthquake rupture to coastal impacts. J. Hydraul. Eng. 149 (9), 04023033.
- Yamazaki, Y., Cheung, K.F., Kowalik, Z., 2011. Depth-integrated, non-hydrostatic model with grid nesting for tsunami generation, propagation, and run-up. Int. J. Numer. Meth. Fluids 67, 2081-2107.
- Yamazaki, Y., Cheung, K.F., Lay, T., 2018. A self-consistent fault-slip model for the 2011 Tohoku earthquake and tsunami. J. Geophys. Res. Solid Earth 123 (2), 1435-1458.
- Yamazaki, Y., Kowalik, Z., Cheung, K.F., 2009. Depth-integrated, non-hydrostatic model for wave breaking and run-up. Int. J. Num. Meth. Fluids 61, 473-497.

Supplementary Material for

A Great Tsunami Earthquake Component of the 1957 Aleutian Islands Earthquake

Yoshiki Yamazaki^a, Thorne Lay^b, Kwok Fai Cheung^{a,*}, Robert C. Witter^c, SeanPaul M. La Selle^d, and Bruce E. Jaffe^d

^aDepartment of Ocean and Resources Engineering, University of Hawai'i at Mānoa, Honolulu, HI 96822, USA

^bDepartment of Earth and Planetary Sciences, University of California Santa Cruz, Santa Cruz, CA 95064, USA

^cU.S. Geological Survey, Alaska Science Center, Anchorage, AK 99508, USA

^d U.S. Geological Survey, Pacific Coastal and Marine Science Center, Santa Cruz, CA 95060, USA.

This PDF file includes:

Figs. S1 to S5

Movie S1.

^{*}Corresponding author. E-mail: cheung@hawaii.edu

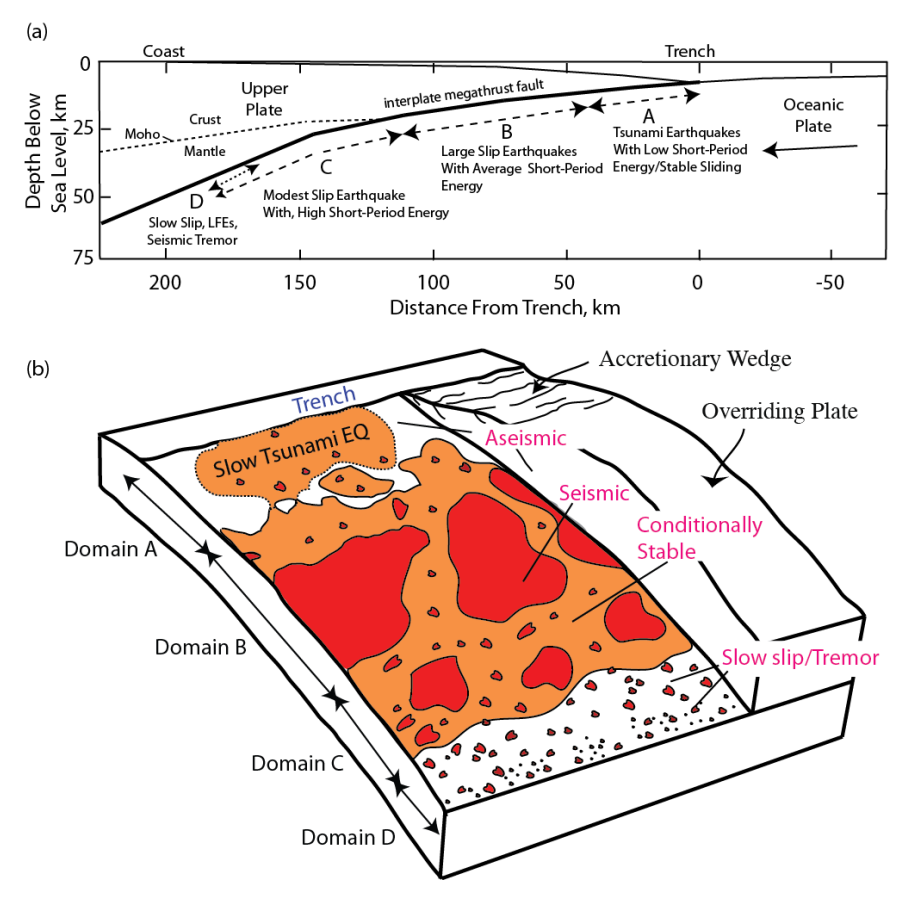


Fig. S1. Rupture Domains along megathrust faults. (a) Schematic cross-section, scaled appropriately for the subduction zone off the northeast coast of Honshu where the great 2011 Tohoku earthquake occurred, indicating four domains of megathrust rupture characteristics: A – near-trench domain where tsunami earthquakes or anelastic deformation and stable sliding occur; B – central megathrust domain where large slip occurs with average short-period seismic radiation; C – down-dip domain where moderate slip occurs with high coherent short-period seismic radiation; D – transitional domain, only present in some areas, typically with a young subducting plate, where slow slip events, low frequency earthquakes (LFEs), and seismic tremor can occur. At yet greater depths the megathrust slides stably or with episodic slow slip or plastic deformation that does not generate earthquakes. (b) Cut-away schematic characterization of the megathrust frictional environment, related to Domains A, B, C and D defined in (a). Regions of unstable frictional sliding are red regions labeled "seismic". Regions of aseismic stable or episodic sliding are white regions labeled "aseismic". Orange areas are conditional stability regions, which displace aseismically except when accelerated by failure of adjacent seismic patches. Domain A is at shallow depth where sediments and pore fluids cause very slow rupture expansion even if large displacements occur in tsunami earthquakes. Domain B has large, relatively uniform regions of stable sliding that can have large slip, but generate modest amounts of short-period radiation upon failure. Domain C has patchy, smaller scale regions of stable sliding surrounded by conditionally stable areas. When these areas fail, coherent short-period radiation is produced. Small, isolated patches may behave as repeaters when quasi-static sliding of surrounding regions regularly loads them to failure. Domain D is dominated by aseismic sliding, but many small unstable patches can rupture in seismic tremor when slow slip events occur. Modified from Lay et al. (2012).

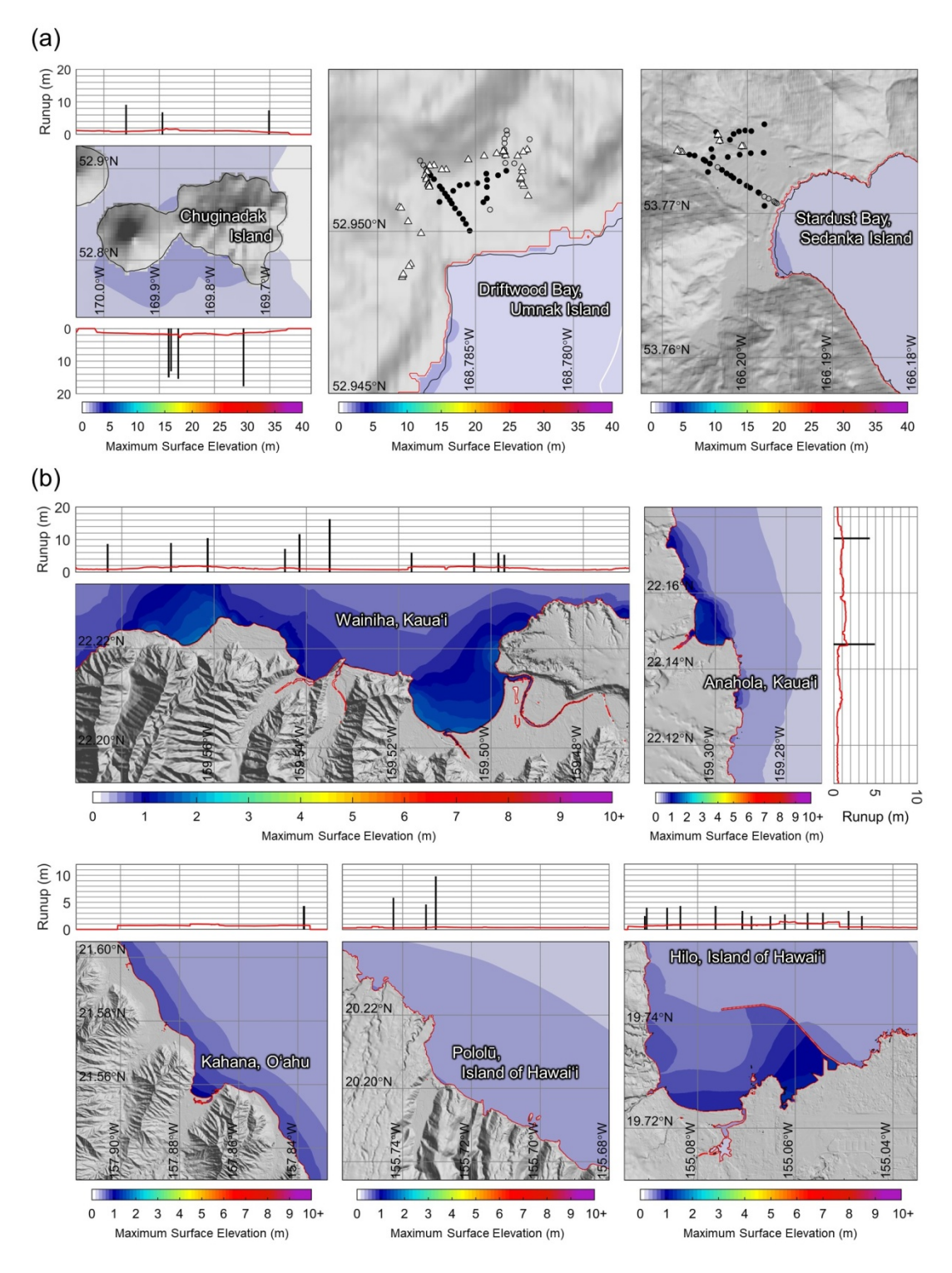


Fig. S2. Inundation and runup comparisons for Model 1957-J1994-T. (a) Aleutian sites. (b) Hawai'i sites. White triangles indicate observed drift log locations; solid and open black circles denote cores with and without deposits. Black bars denote observed maximum deposit elevations on Chuginadak Island from Griswold et al. (2019) and observed runup heights at Hawai'i sites from Walker (2004). Black lines denote waterlines at local MSL and red lines delineate computed runup heights and inundation limits.

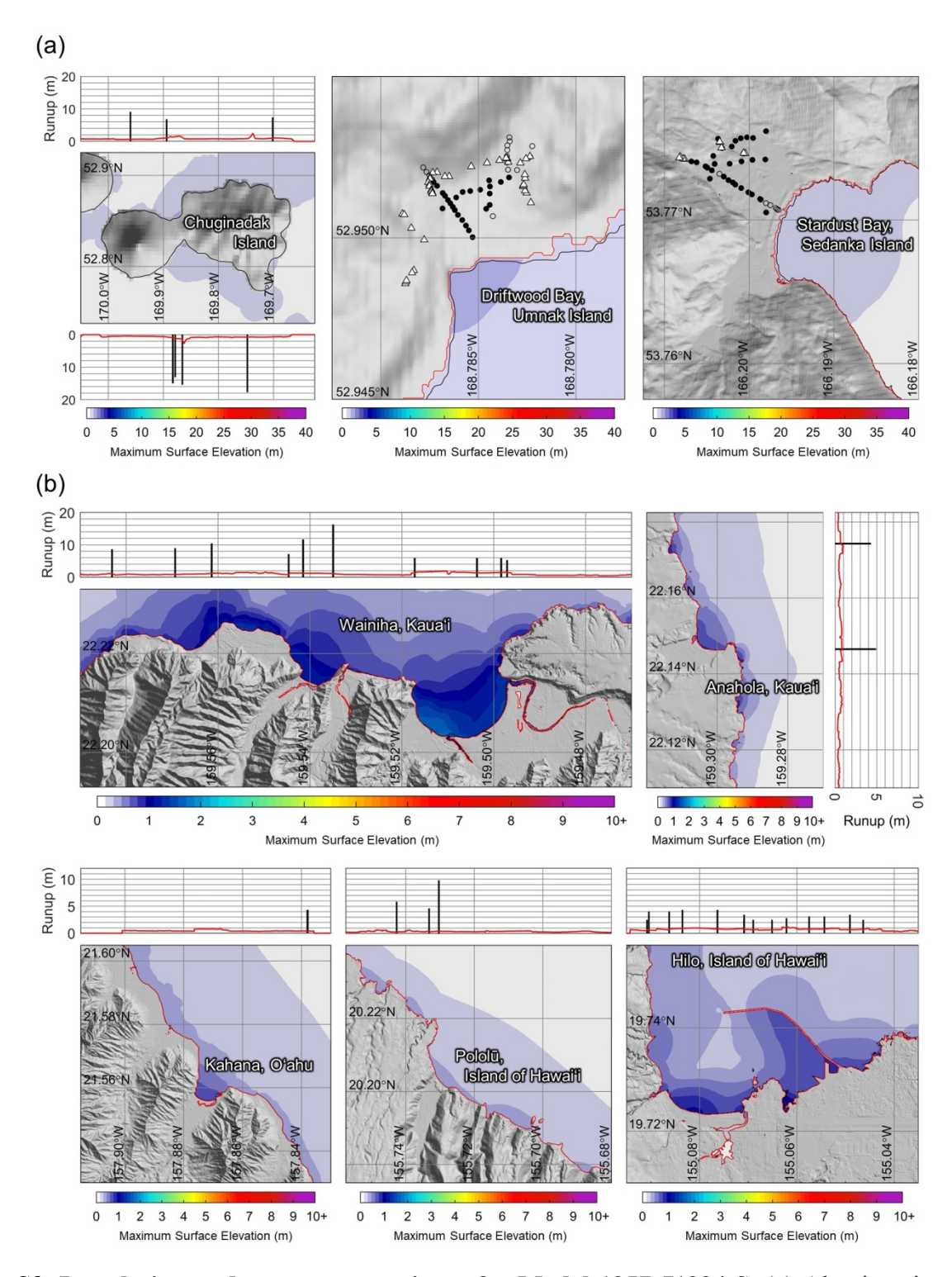


Fig. S3. Inundation and runup comparisons for Model 1957-J1994-S. (a) Aleutian sites. (b) Hawai'i sites. White triangles indicate observed drift log locations; solid and open black circles denote cores with and without deposits. Black bars denote observed maximum deposit elevations on Chuginadak Island from Griswold et al. (2019) and observed runup heights at Hawai'i sites from Walker (2004). Black lines denote waterlines at local MSL and red lines delineate computed runup heights and inundation limits.

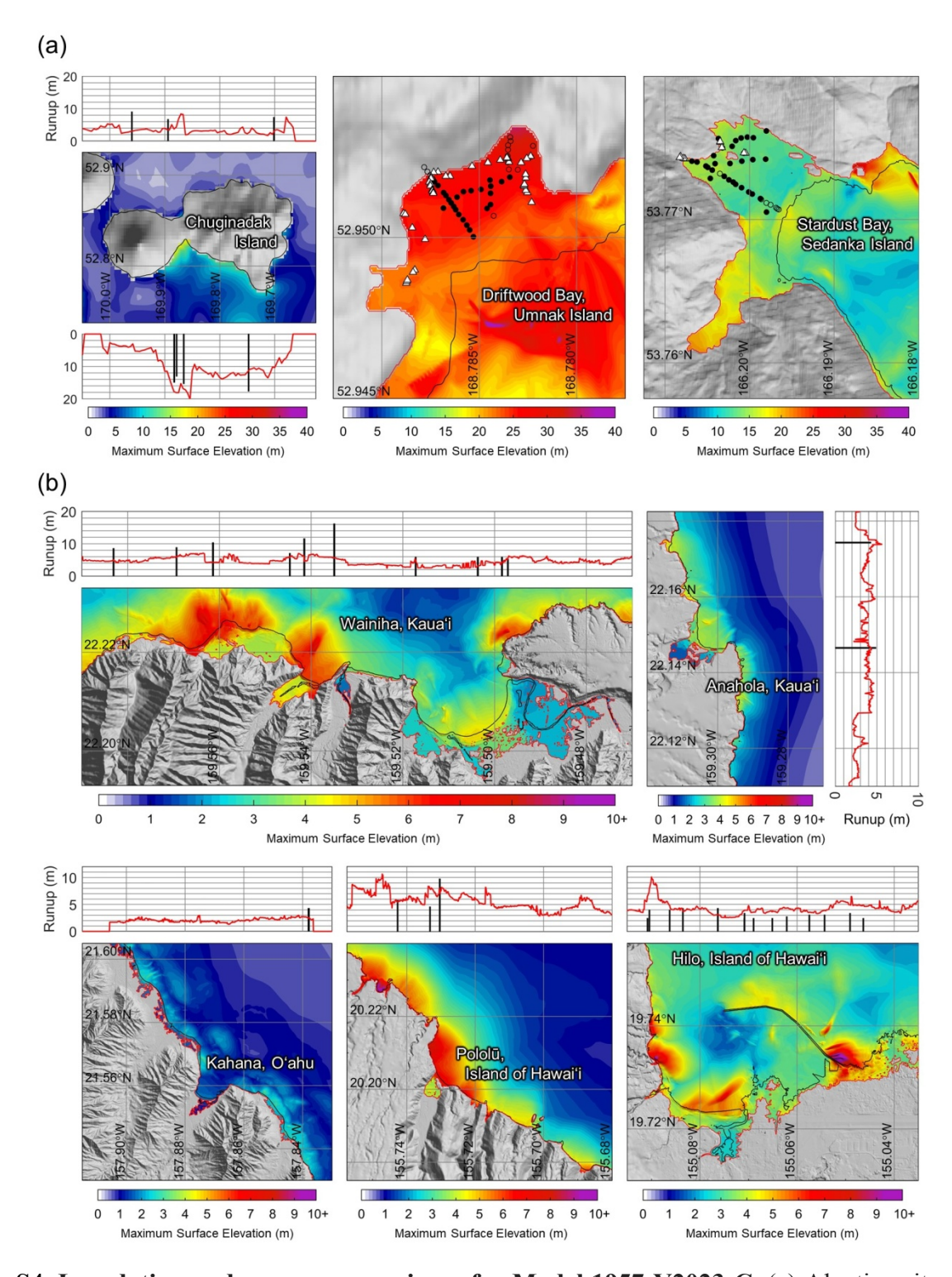


Fig. S4. Inundation and runup comparisons for Model 1957-Y2023-C. (a) Aleutian sites. (b) Hawai'i sites. White triangles indicate observed drift log locations; solid and open black circles denote cores with and without deposits. Black bars denote observed maximum deposit elevations on Chuginadak Island from Griswold et al. (2019) and observed runup heights at Hawai'i sites from Walker (2004). Black lines denote waterlines at local MSL and red lines delineate computed runup heights and inundation limits.

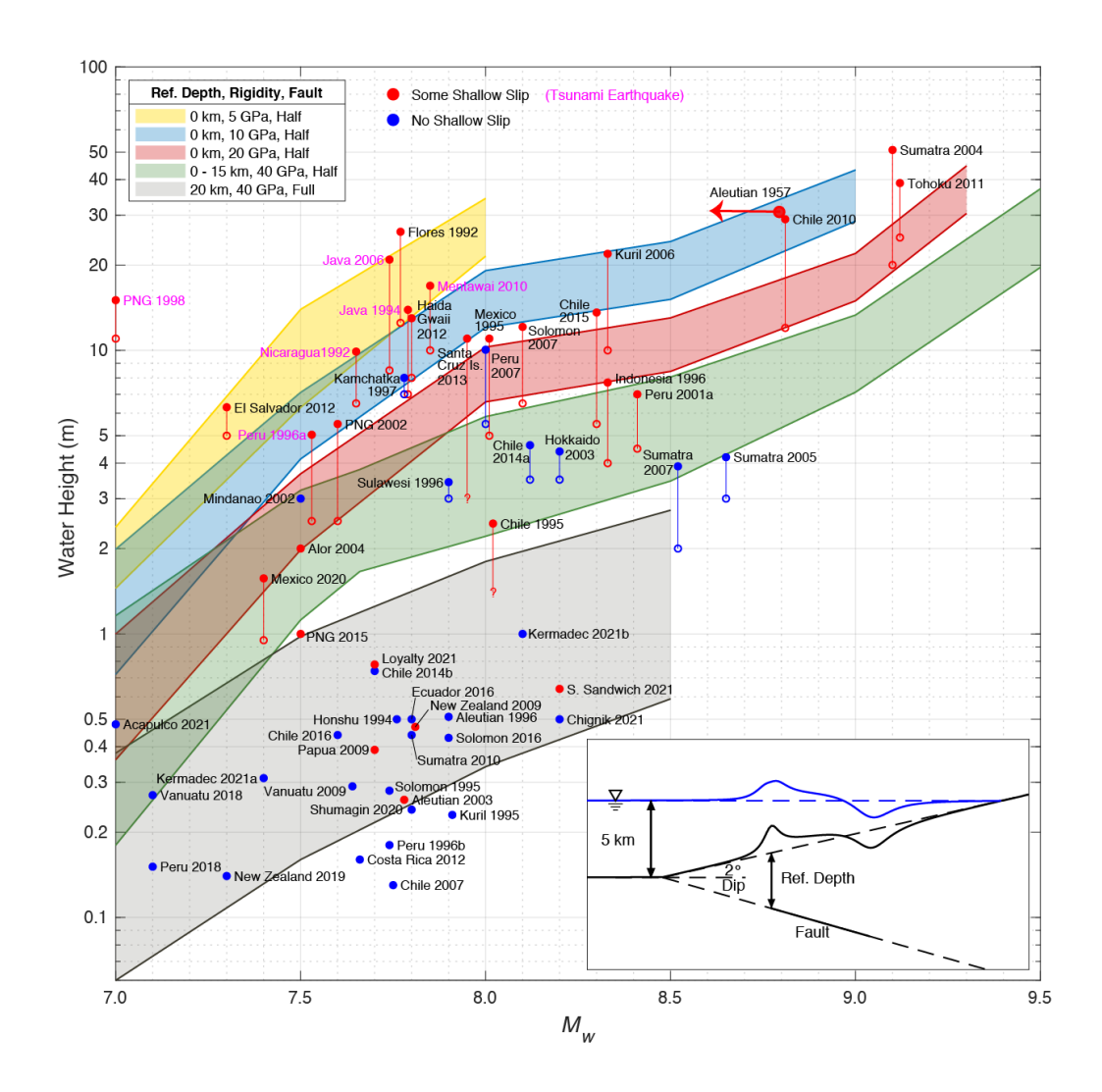
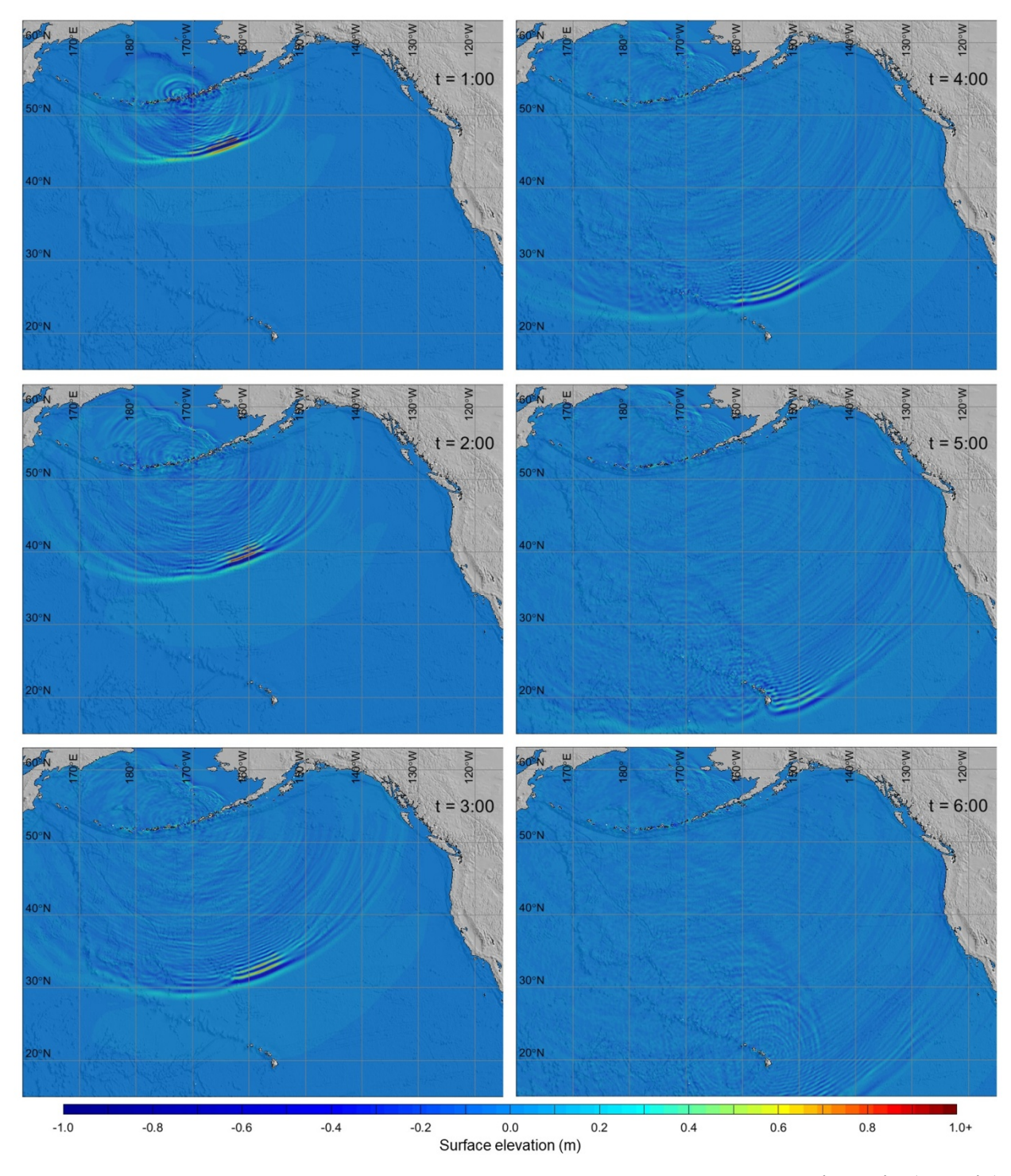


Fig. S5. Water height versus moment magnitude of megathrust earthquakes. Modified from Cheung et al. (2022) to include the 1957 Aleutian earthquake and tsunami. The arrow on the 1957 data point indicates the range of total moment associated with uncertain rigidity of the shallow megathrust where the eastern tsunami earthquake component occurred.



Movie S1. Trans-Pacific tsunami propagation for Model 1957-Y2023-D. Time t in (Hr:Min) after earthquake initiation.